

# Tension-Induced Soft Stress and Viscoelastic Bending in Liquid Crystal Elastomers for Enhanced Energy Dissipation

Beijun Shen<sup>†a,\*</sup>, Yuefeng Jiang<sup>a</sup>, Christopher M. Yakacki<sup>b</sup>, Sung Hoon Kang<sup>a,c,\*</sup>, Thao D. Nguyen<sup>a</sup>

<sup>a</sup>*Department of Mechanical Engineering, Johns Hopkins University, Baltimore, Maryland 21218, United States of America*

<sup>b</sup>*Department of Mechanical Engineering, University of Colorado, Denver, CO 80204, USA*

<sup>c</sup>*Department of Materials Science and Engineering, Korea Advanced Institute of Science and Technology, Daejeon 34141, Republic of Korea*

---

## Abstract

Architected materials that harness elastic snap-through buckling can trap energy reversibly. Liquid crystal elastomers (LCEs) exhibit excellent dissipation capabilities due to polymer network viscoelasticity and rate-dependent soft stress behavior associated with mesogen rotation. Incorporating LCEs into buckling lattice structures enhances energy absorption; however, conventional design cannot take advantage of the dissipation mechanism associated with mesogen rotation because buckling occurs at strains below the threshold of the soft stress response. In this study, we investigate tension-induced mesogen rotation as an additional dissipation mechanism in horizontal members of structures composed of tilted LCE beams under compression. Viscoelastic properties of LCEs with two crosslinking densities were characterized experimentally, and a nonlinear viscoelastic user-defined element was implemented in Abaqus/Standard to capture finite-strain behavior, including soft stress effects. Simulations and experiments revealed a non-monotonic dependence of energy dissipation on the thickness ratio between horizontal and tilted LCE members. Optimized structures with stretchable horizontal bars dissipated 2–3 times more energy than rigid-bar counterparts by balancing tension-driven soft stress with viscoelastic beam bending. Energy contributions from mesogen rotation and polymer network viscoelasticity were quantified. These findings inform the design strategies for LCE-based architected materials to enhance dissipation.

*Keywords:* Liquid crystal elastomers, viscoelasticity, soft elasticity, buckling, energy dissipation

---

---

\*Corresponding authors

*Email addresses:* bs3660@columbia.edu (Beijun Shen<sup>†</sup>), shkang2024@kaist.ac.kr (Sung Hoon Kang)

<sup>†</sup>Beijun Shen has moved to Columbia University

## 1. Introduction

Designing materials and structures for impact mitigation and vibration isolation requires efficient energy absorption. Architected materials that exploit geometric instabilities, such as snap-through buckling, enable reversible energy trapping through large elastic deformations (Shan et al., 2015; Meza et al., 2014; Chen and Jin, 2021; Bertoldi, 2017; Yang and Ma, 2019; Haghpanah et al., 2016; Frenzel et al., 2016). Snap-through instability involves a rapid transition between two elastic equilibria, resulting in simultaneous shape change and unloading (Qiu et al., 2004). The structure stores elastic strain energy in the buckled state until additional energy is applied to restore the original configuration. However, energy absorption in purely elastic bistable structures is rate-independent, limiting their effectiveness under dynamic or impact loading.

To overcome this limitation, recent studies have incorporated rate-dependent dissipation mechanisms, such as viscoelasticity, into bistable systems (Jeon et al., 2022; Liu et al., 2024; Li et al., 2022; Valizadeh and Weeger, 2024; Yao et al., 2024; Liu et al., 2022). Among viscoelastic materials, liquid crystal elastomers (LCEs) are particularly promising due to the coupling between polymer network deformation and mesogen rotation. LCEs consist of crosslinked polymer networks embedded with stiff, rod-like mesogens aligned along a preferred direction (the director). This coupling gives rise to reversible actuation (Warner and Terentjev, 2003; Küupfer and Finkelmann, 1994), soft stress behavior (Azoug et al., 2016; Martin Linares et al., 2020), and enhanced dissipation (Clarke et al., 2001; Merkel et al., 2019). Compared to conventional elastomers, LCEs exhibit elevated loss factors over a broad frequency and temperature range and pronounced hysteresis under cyclic loading, driven by both polymer network viscoelasticity and mesogen reorientation (Azoug et al., 2016; Martin Linares et al., 2020; Clarke et al., 2001; Merkel et al., 2019; Traugutt et al., 2020; Shen, 2025).

Soft stress arises when mesogens rotate under loading, typically in polydomain or monodomain LCEs with directors initially perpendicular to the applied strain (Azoug et al., 2016; Martin Linares et al., 2020; Merkel et al., 2018; Clarke et al., 1998; Takebe and Urayama, 2020; Mistry et al., 2021). The stress-strain response exhibits an initial linear regime up to peak stress, followed by a softening plateau due to viscous mesogen rotation and a stiffening regime associated with chain alignment. These features are often accompanied by significant hysteresis and inelastic strain upon unloading, making soft stress a powerful dissipation mechanism at finite strain rates.

In previous work, we developed architected lattices composed of repeating unit cells with tilted LCE beams sandwiched between rigid horizontal supports (Jeon et al., 2022). These structures combined snap-through buckling and LCE viscoelasticity to enhance energy absorption. While they exhibited snap-through transitions, the buckled shape was maintained for an extended period and gradually recovered due to viscoelastic relaxation. During this time, the reaction force remained nonzero, indicating pseudo-bistability (Brinkmeyer et al., 2013; Gomez et al., 2019; Che et al., 2019; Chen et al., 2022). However, strains in the tilted beams during buckling remained below 30–40%, insufficient to activate soft stress via mesogen rotation. Because this rotation is largely irreversible, its activation offers potential for significantly greater energy dissipation. Mistry et al. (Mistry et al., 2021) reported plateau-like soft

stress enabling impact absorption at nearly constant stress, and Shaha et al. (Shaha et al., 2020) observed stronger soft stress under transverse tension than longitudinal compression, likely due to increased mesogen reorientation.

Despite this promise, the use of soft stress for structural-scale dissipation remains largely unexplored. Luo et al. (Luo et al., 2021) indirectly investigated this mechanism by showing that increased lattice connectivity ( $Z$ ) in polydomain LCE foams enhanced energy dissipation, which they attributed to greater axial strain and possible mesogen rotation, though this was not directly measured. Related studies on bi-material lattices incorporated rigid inclined struts connected to highly extensible transverse elements (Ye et al., 2023; Ruschel and Zok, 2020). These systems absorb energy through axial stretching of the transverse strut under vertical compression while suppressing buckling in the inclined beams. Moreover, the materials used in these studies were conventional elastomers, such as thermoplastic polyurethane (TPU), rather than LCEs. As a result, they did not exploit the soft stress mechanism, which is unique to LCEs and enables energy dissipation through mesogen rotation, nor did they combine it with viscoelastic bending.

Here, we introduce tension-induced soft stress in LCEs as an active dissipation mechanism in bistable LCE structures subjected to macroscopic compression. Building on our previous design (Jeon et al., 2022), we replace the rigid horizontal member with a stretchable LCE bar. Under compression, the tilted beams bend while the horizontal bar stretches, activating soft stress through mesogen rotation. However, lateral expansion of the stretched bar reduces the tilt angle, diminishing bending and its associated dissipation. This tradeoff creates a nonlinear interaction between viscoelastic bending and soft-stress-driven stretching. We systematically investigate this interplay using finite element simulations and experiments, varying LCE material properties and the thickness ratio between horizontal and tilted members. A nonlinear viscoelastic user-defined element (UEL) was implemented in Abaqus/Standard to capture finite strain behavior, including soft stress from mesogen rotation. Energy contributions from mesogen rotation and polymer network viscoelasticity were quantitatively assessed. Our results reveal a non-monotonic dependence of energy dissipation on the thickness ratio, with maximum absorption achieved at an intermediate value. Optimized structures dissipated two to three times more energy than those with rigid bars, demonstrating the synergistic benefit of combining viscoelastic bending and tension-induced soft stress.

## 2. Methods

### 2.1. Experimental Methods

#### 2.1.1. LCE material preparation

Impressio (Denver, CO, USA) synthesized and supplied two sets of LCEs with different crosslinking densities, formulated to replicate the chemical, mechanical, and morphological behavior reported in prior studies (Yakacki et al., 2015; Saed et al., 2017). The fabrication process involved a two-stage thiol-acrylate Michael addition, mechanical alignment, and subsequent photopolymerization to produce main-chain monodomain LCEs. Polydomain LCEs were fabricated using the same procedure but without mechanical alignment. The precursor mixture consisted of 2,2'-(Ethylenedioxy)diethanethiol (EDDET), Pentaerythritol tetrakis(3-mercaptopropionate) (PETMP), and 1,4-Bis-[4-(3-acryloyloxypropoxy)benzoyloxy]-2-methylbenzene

(RM257). Two batches of polydomain LCEs with varying crosslinking densities were prepared. To obtain monodomain LCEs, approximately 100% strain was applied to half of the polydomain samples from each batch, aligning the mesogens through a nematic phase transition via director rotation. The resulting polydomain sheets had an average thickness of approximately 0.93 mm, and the monodomain sheets measured approximately 0.64 mm. The specific catalysts, initiators, and processing conditions remain proprietary to Impressio.

### 2.1.2. Unit cell structure preparation

Unit cell structures were fabricated using LCEs with different crosslinking densities (Figure 1). LCE strips were cut from prepared sheets to specified dimensions. Two types of strips were used: polydomain LCEs and monodomain LCEs, the latter featuring an initial director perpendicular to the longitudinal axis (hereafter referred to as perpendicular LCEs). Each unit cell consisted of four identical tilted LCE beams arranged in a hexagonal configuration and a horizontal transverse member, whose material and thickness varied across designs. This layout enabled a systematic investigation of how material and geometric parameters influence mechanical response and energy dissipation. All components were assembled using 3D-printed rigid joints made from Rigid 10K Resin (FormLab 2B, Formlabs Inc., Somerville, MA, USA) and bonded with Gorilla Super Glue (Cincinnati, OH, USA). The adhesive was cured overnight before testing.

Each unit cell had an in-plane width of approximately 30 mm. The total height was approximately 35 mm for the structures shown in Figure 1a, b, d, and e, and about 37 mm for the one in Figure 1c. The out-of-plane thickness was 5 mm for all designs. Each tilted LCE beam had an effective length of 13.4 mm, a thickness of 0.93 mm, and was oriented at a  $60^\circ$  angle relative to the horizontal member. All tilted beams were composed of polydomain LCE with higher crosslinking density. The  $60^\circ$  inclination was chosen to balance competing effects. Larger angles reduce the horizontal force component available to stretch the horizontal member, whereas smaller angles limit vertical displacement under compression, thereby diminishing both beam bending and horizontal stretching.

The horizontal member, when present, had an effective length of 8 mm and an out-of-plane thickness of 5 mm. Its thickness and material were varied across five unit cell configurations. Unit cell 1 included a perpendicular LCE bar with lower crosslinking density and a thickness of 0.64 mm. Unit cell 2 used a rigid bar of the same thickness made from Rigid 10K Resin to constrain deformation. Unit cell 3 maintained the same LCE formulation as unit cell 1 but doubled the thickness to 1.28 mm by bonding two identical strips using 3M™ VHB™ Tape F9460PC. Unit cell 4 employed a perpendicular LCE bar with higher crosslinking density and a thickness of 0.64 mm, enabling direct comparison with unit cell 1 to isolate the effect of crosslinking density. Unit cell 5 omitted the horizontal member entirely, serving as a control to assess its contribution to mechanical performance. In all cases where LCE horizontal bars were used, the initial director was perpendicular to the longitudinal direction and oriented into the page in Figure 1. Table 1 summarizes the configurations.

To eliminate residual strain from fabrication and handling, all unit cells underwent thermal resetting. Structures were heated on a hot plate at  $125^\circ\text{C}$  – above the LCE nematic-to-isotropic transition temperature for 5 minutes and then cooled to room temperature for at

least 20 minutes. This treatment ensured a uniform initial state prior to mechanical testing. Following thermal resetting, the unit cells were subjected to vertical compression to evaluate their mechanical response and energy dissipation.

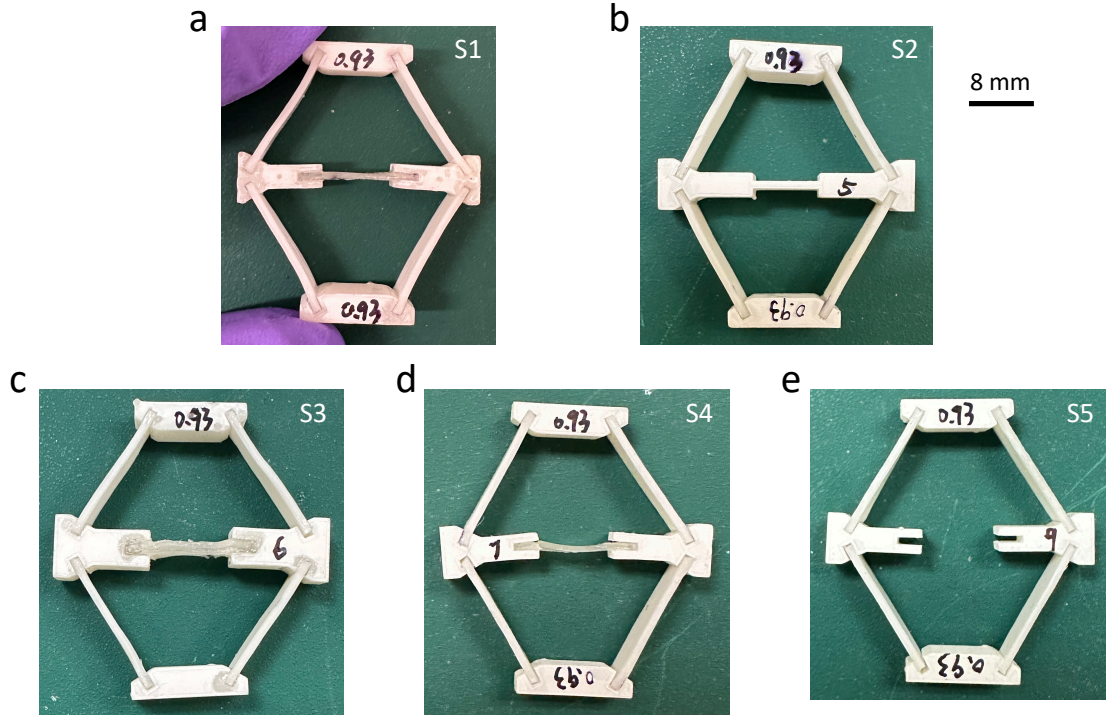


Figure 1: Experimental unit cell structures. All tilted beams are composed of polydomain LCE with higher crosslinking density and are oriented at  $60^\circ$  relative to the horizontal bar. (a) Unit cell 1: perpendicular LCE, lower crosslinking density, 0.64 mm thickness. (b) Unit cell 2: rigid horizontal bar, 0.64 mm thickness. (c) Unit cell 3: perpendicular LCE, lower crosslinking density, 1.28 mm thickness. (d) Unit cell 4: perpendicular LCE, higher crosslinking density, 0.64 mm thickness. (e) Unit cell 5: no horizontal bar.

Table 1: Summary of unit cell configurations. The tilted beams were composed of polydomain LCE with higher crosslinking density and a thickness of 0.93 mm.

Unit cell	Horizontal member	Thickness (mm)
Unit cell 1	Lower CLD, $\perp$	0.64
Unit cell 2	Rigid	0.64
Unit cell 3	Lower CLD, $\perp$	1.28
Unit cell 4	Higher CLD, $\perp$	0.64
Unit cell 5	None	–

### 2.1.3. Dynamic mechanical analysis (DMA) tests

Dynamic mechanical analysis was conducted using a DMA 850 (TA Instruments, New Castle, DE, USA) equipped with a liquid nitrogen cooling system to characterize the viscoelastic properties of both monodomain and polydomain LCEs. LCE sheets were cut into strips measuring 20 mm in length and approximately 9 mm in width. Each specimen was mounted

in tension clamps with an active length of 5–10 mm and subjected to sinusoidal dynamic strain with an amplitude of 0.1%. Oscillatory temperature and frequency sweeps were performed to evaluate the viscoelastic response. The temperature was increased from  $-40\text{ }^{\circ}\text{C}$  to  $150\text{ }^{\circ}\text{C}$  in  $5\text{ }^{\circ}\text{C}$  increments. At each temperature, frequency sweeps ranging from 0.02 Hz to 20 Hz were conducted to measure the storage modulus ( $E'$ ) and loss modulus ( $E''$ ). Samples were held isothermally for 5 minutes before data acquisition at each temperature to ensure thermal equilibrium. Before testing, all specimens were thermally reset by heating at  $125\text{ }^{\circ}\text{C}$  for 5 minutes, then cooling to room temperature for at least 20 minutes to eliminate residual strains and establish consistent initial conditions. Master curves for storage modulus and  $\tan\delta$  were constructed by horizontally shifting the frequency sweep data using the time–temperature superposition (TTS) principle, referenced to  $25\text{ }^{\circ}\text{C}$  (Ferry, 1980).

#### *2.1.4. Uniaxial tension load-unload tests*

The large-strain viscoelastic behavior of LCEs was characterized through uniaxial tension load–unload tests. Monodomain LCE strips were cut to 50 mm in length, 10 mm in width, and 0.64 mm in thickness, with the long axis either parallel or perpendicular to the pre-stretch direction. Approximately 10 mm at each end was reserved for gripping, leaving a 10 mm gauge length at the center, which was marked with a black permanent marker for strain tracking. Quasi-static tests were performed under displacement control using an MTS Insight 5 universal testing machine equipped with a 500 N load cell (MTS Systems, Eden Prairie, MN, USA). Specimens were mounted between tensile grips, and a preload of 0.06 N was applied to remove slack. This value was determined based on observed load fluctuations at zero force. For each crosslinking density, three specimens were tested in both parallel and perpendicular orientations to assess variability. Tests were conducted at four strain rates (0.01%/s, 0.1%/s, 1%/s, and 10%/s) to capture rate-dependent behavior. Prior to testing, all samples were thermally reset by heating at  $125\text{ }^{\circ}\text{C}$  for 5 minutes, followed by cooling at room temperature for at least 20 minutes to ensure consistent initial conditions. Target strains varied with crosslinking density and orientation. Perpendicular specimens were stretched to capture both the soft stress plateau associated with mesogen rotation and the strain-stiffening regime due to polymer chain alignment. To avoid fracture, specimens with lower and higher crosslinking densities were stretched to 800% and 700% engineering strain, respectively. Parallel LCEs were stretched to 80% and 70% strain for the lower and higher crosslinking density, respectively. Engineering stress was calculated as the reaction force divided by the initial cross-sectional area, and engineering strain as the applied displacement divided by the gauge length. Young’s modulus was determined from a linear fit to the initial 5% strain range. For perpendicular LCEs, peak stress was defined as the maximum stress preceding strain softening. Hysteresis was quantified by numerically integrating the enclosed area within the stress–strain loop using the trapezoidal rule.

#### *2.1.5. Compression tests of unit cell structures*

Quasi-static uniaxial compression tests were conducted to evaluate the mechanical response and energy absorption of the unit cell structures and to validate finite element simulations. Tests were performed under displacement control using an MTS Insight 5 universal testing machine equipped with a 100 N load cell (MTS Systems, Eden Prairie, MN, USA). Each unit cell was positioned between two rigid cylindrical plugs, each 12 mm in diameter and

15 mm in height, fabricated from Rigid 10K Resin (FormLab 2B, Formlabs Inc., Somerville, MA, USA). The lower plug was affixed to the bottom compression plate using double-sided tape to prevent sliding, while the upper plug was mounted to the upper compression plate to ensure symmetric loading. This plug–unit cell–plug configuration prevented mechanical interference between the unit cell and the platens during compression.

Prior to testing, each unit cell was thermally reset following the procedure in Section 2.1.2 to eliminate residual strains and ensure consistent initial conditions. The upper platen was manually lowered until the upper plug contacted the top surface of the unit cell without inducing deformation. The load cell was then zeroed, and compression was initiated. Tests were performed at three effective strain rates: 1%/s, 10%/s, and 50%/s. Each unit cell was compressed to a total displacement of 20 mm. The corresponding displacement rates were calculated by multiplying the strain rate by the target displacement to maintain consistency across tests. Crosshead displacement was recorded as the applied displacement, and the load cell measured the reaction force. Each configuration was tested three times at each strain rate to evaluate repeatability and variability. Energy absorption was computed by numerically integrating the area under the load-displacement curve using the trapezoidal rule.

## 2.2. Modeling Methods

### 2.2.1. Finite deformation quasi-linear viscoelastic model

Compression of the unit cell structures induces bending in the tilted beams, generating tensile strains below 40%, which are below the threshold for semi-soft stress associated with mesogen rotation in perpendicular-loaded LCEs. In this moderate strain regime, the material exhibits classical viscoelastic behavior. We modeled this response using the finite-deformation viscoelastic formulation available in Abaqus/Standard (Dassault Systèmes, 2023).

This viscoelastic framework assumes that the strain and time dependence of the stress response are separable. The total stress is decomposed into a time-independent hyperelastic component and a time-dependent viscoelastic contribution governed by a dimensionless shear relaxation function  $g(t)$ , defined as:

$$g(t) = \frac{\mu(t)}{\mu_0}, \quad (1)$$

where  $\mu(t)$  is the shear modulus at time  $t$ , and  $\mu_0 = \mu(0)$  is the instantaneous shear modulus. By definition,  $g(0) = 1$  and  $g(\infty) = \mu_\infty/\mu_0$ , where  $\mu_\infty$  denotes the long-term (equilibrium) shear modulus. The relaxation function is approximated using a Prony series:

$$g(t) = g_\infty + \sum_{i=1}^N g_i e^{-t/\tau_i}, \quad (2)$$

where  $g_\infty = \mu_\infty/\mu_0$ ,  $\tau_i$  are characteristic relaxation times, and the coefficients satisfy  $\sum_{i=1}^N g_i = 1 - g_\infty$ . These parameters were calibrated by fitting the DMA-derived master curves of the storage modulus under uniaxial tension (Section 2.1.3). The full calibration procedure and final parameter values are detailed in Appendix E.

The dimensionless relaxation function  $g(t)$  enters the hereditary integral formulation of the Cauchy stress:

$$\begin{aligned}\boldsymbol{\sigma}(\mathbf{F}, t) &= \boldsymbol{\sigma}^D(\bar{\mathbf{F}}, t) + \boldsymbol{\sigma}^H(J), \\ \boldsymbol{\sigma}^D(\mathbf{F}, t) &= \boldsymbol{\sigma}_0^D(\mathbf{F}(t)) + \text{dev} \left[ \int_0^t \dot{g}(t') \bar{\mathbf{F}}_t^{-1}(t-t') \cdot \boldsymbol{\sigma}_0^D(\mathbf{F}(t-t')) \cdot \bar{\mathbf{F}}_t^{-\top}(t-t') dt' \right],\end{aligned}\quad (3)$$

where  $\boldsymbol{\sigma}$  is the total Cauchy stress, decomposed into deviatoric and volumetric components,  $\boldsymbol{\sigma}^D$  and  $\boldsymbol{\sigma}^H$ , respectively. The quantity  $\boldsymbol{\sigma}_0^D$  denotes the instantaneous deviatoric Cauchy stress,  $\mathbf{F}$  is the deformation gradient,  $J = \det(\mathbf{F})$  is the volume ratio, and  $\bar{\mathbf{F}} = J^{-1/3}\mathbf{F}$  is the distortional (isochoric) part of  $\mathbf{F}$ . The tensor  $\bar{\mathbf{F}}_t(t-t')$  denotes the relative distortional deformation gradient from time  $t-t'$  to  $t$ . The deviatoric projection is defined as  $\text{dev}(\mathbf{A}) = \mathbf{A} - \frac{1}{3}\text{tr}(\mathbf{A})\mathbf{I}$ . For simplicity, the volumetric response  $\boldsymbol{\sigma}^H$  is assumed time-independent.

To define the rate-independent elastic response, we employed a hyperelastic model. In Abaqus, this model may be applied to either the instantaneous stress  $\boldsymbol{\sigma}_0^D$  or the equilibrium stress  $\boldsymbol{\sigma}_\infty^D$ . We chose the latter, since the long-time, high-temperature equilibrium state is clearly identifiable in the DMA-measured storage modulus. The deviatoric equilibrium Cauchy stress is computed from the hyperelastic strain energy density:

$$\boldsymbol{\sigma}_\infty^D = \frac{2}{J} \text{dev} \left[ \left( \frac{\partial W}{\partial \bar{I}_1} + \bar{I}_1 \frac{\partial W}{\partial \bar{I}_2} \right) \bar{\mathbf{B}} - \frac{\partial W}{\partial \bar{I}_2} \bar{\mathbf{B}}^2 \right], \quad (4)$$

where  $\bar{\mathbf{B}} = \bar{\mathbf{F}}\bar{\mathbf{F}}^\top$  is the deviatoric left Cauchy–Green tensor, and  $\bar{I}_1, \bar{I}_2$  are its first and second invariants.

For simplicity, we adopted the built-in compressible neo-Hookean model in Abaqus to define the hyperelastic strain energy density:

$$W = C_1(\bar{I}_1 - 3) + \frac{1}{D_1}(J - 1)^2, \quad (5)$$

where  $2C_1 = \mu_\infty$  and  $D_1 = 2/K$ , with  $\mu_\infty$  denoting the equilibrium shear modulus and  $K$  the bulk modulus. The equilibrium shear modulus is related to the instantaneous modulus by:

$$\mu_\infty = \mu_0 \left( 1 - \sum_{i=1}^N g_i \right). \quad (6)$$

We estimated  $\mu_\infty = 0.666$  MPa from the low-frequency (rubbery plateau) storage modulus measured via DMA for the polydomain LCE with higher crosslinking density. The bulk modulus was specified as  $K = 8733.6$  MPa, calculated from the high-frequency (glassy) storage modulus  $E^{\text{neq}}$  using

$$K = \frac{E^{\text{neq}}}{3(1 - 2\nu_g)}, \quad (7)$$

where  $\nu_g = 0.35$  is the assumed Poisson's ratio in the glassy regime. This physically motivated choice yields a bulk modulus over five orders of magnitude greater than  $\mu_\infty$ , ensuring a nearly incompressible response.

### 2.2.2. Finite Deformation Viscoelastic Micropolar Model for Monodomain LCEs

The finite deformation micropolar viscoelastic theory developed by Wang et al. (2022) was used to model the anisotropic, large-deformation behavior of monodomain LCEs. We briefly summarize the constitutive model below. The theory conceptualizes a monodomain as a continuum with a director field  $\mathbf{d}$  that can rotate independently of the deformation gradient  $\mathbf{F}$ . The director describes the mean preferred orientation of the mesogens. The degree of alignment is described by the order parameter,  $Q$ , which is assumed to be constant and independent of deformation. The network deformation tensor is defined as,  $\mathbf{F}_N = \mathbf{l}^{-\frac{1}{2}} \mathbf{F} \mathbf{l}_0^{\frac{1}{2}}$ , to represent the deformation of the polymer network relative to the deformation caused by director rotation, and the current  $\mathbf{l}$  and reference  $\mathbf{l}_0$  step length tensors are defined as,

$$\mathbf{l} = (1 - Q) (\mathbf{I} - \mathbf{d} \otimes \mathbf{d}) + (1 + 2Q) \mathbf{d} \otimes \mathbf{d}, \quad (8)$$

$$\mathbf{l}_0 = (1 - Q) (\mathbf{I} - \mathbf{d}^0 \otimes \mathbf{d}^0) + (1 + 2Q) \mathbf{d}^0 \otimes \mathbf{d}^0, \quad (9)$$

where  $\mathbf{d}^0$  is the reference director orientation.

To describe the viscoelastic deformation of the material, a multiplicative decomposition was assumed for the deformation gradient into elastic and viscous parts,  $\mathbf{F} = \mathbf{F}^e \mathbf{F}^v$ . This allows the elastic network deformation to be defined as,  $\mathbf{F}_N^e = \mathbf{l}^{-\frac{1}{2}} \mathbf{F}^e \mathbf{l}_0^{\frac{1}{2}}$ ,

The following free energy density was assumed for the viscoelastic stress response of the network:

$$\Psi(\mathbf{F}_N, \mathbf{F}_N^e, J, \mathbf{d}) = \bar{\Psi}^{\text{eq}}(\mathbf{F}_N) + \bar{\Psi}^{\text{neq}}(\mathbf{F}_N^e) + \frac{\kappa}{2}(J - 1)^2 + \frac{\gamma}{4}(\mathbf{d} \cdot \mathbf{d} - 1)^2, \quad (10)$$

where  $\kappa$  is the bulk modulus of the LCE material, was set to be 1000 times the shear modulus at equilibrium to approximate an incompressible deformation response and  $\gamma$  is a Lagrange multiplier constraining  $\mathbf{d} \cdot \mathbf{d} = 1$ . The neo-Gent model was introduced by Wang et al. (2022) for the equilibrium and non-equilibrium free energy densities to describe the strain stiffening stress response of the polymer network at large deformation. The individual components are:

$$\begin{aligned} \bar{\Psi}^{\text{eq}} &= -\frac{\mu^{\text{eq}}}{2} I_m \ln \left( 1 - \frac{I^N - 3}{I_m} \right) - \mu^{\text{eq}} \ln J, \\ \bar{\Psi}^{\text{neq}} &= -\frac{\mu^{\text{neq}}}{2} I_m \ln \left( 1 - \frac{I^{Ne} - 3}{I_m} \right) - \mu^{\text{neq}} \ln J^e, \end{aligned} \quad (11)$$

where  $J = \det(\mathbf{F})$ ,  $J^e = \det(\mathbf{F}^e)$ ,  $I^N$  and  $I^{Ne}$  are the first invariants of  $\mathbf{C}_N = \mathbf{F}_N^\top \mathbf{F}_N$  and  $\mathbf{C}_N^e = \mathbf{F}_N^{e\top} \mathbf{F}_N^e$ ,  $\mu^{\text{eq}}$  and  $\mu^{\text{neq}}$  are the equilibrium and nonequilibrium shear moduli, and  $I_m$  is the strain stiffening parameter. Neglecting the effects of director gradients, the constitutive equations for the stress response, evolution of the viscous deformation gradient, and evolution of the director field are defined from the free energy density as follows:

$$\boldsymbol{\sigma} = \frac{1}{J} \text{sym} \left( \frac{\partial \Psi}{\partial \mathbf{F}} \mathbf{F}^\top + \frac{\partial \Psi}{\partial \mathbf{F}^e} \mathbf{F}^{e\top} \right) \quad (12)$$

$$\mathbf{L}^v = \frac{1}{\eta_N} \mathbf{F}^{e\top} \frac{\partial \Psi}{\partial \mathbf{F}^e}, \quad (13)$$

$$\dot{\mathbf{d}} - \mathbf{W} \mathbf{d} = -\frac{1}{J \eta_D} \left[ \frac{\partial \Psi}{\partial \mathbf{d}} - \left( \frac{\partial \Psi}{\partial \mathbf{d}} \cdot \mathbf{d} \right) \mathbf{d} \right]. \quad (14)$$

Here,  $\mathbf{L}^v = \dot{\mathbf{F}}^v \mathbf{F}^{v-1}$  is the viscous rate of deformation tensor,  $\mathbf{W}$  is the spin tensor,  $\eta_D$  and  $\eta_N$  are the viscosities associated with director rotation and viscous deformation of the polymer network, respectively.

Substituting equations (10) and (11) into (12) gives the Cauchy stress:

$$\boldsymbol{\sigma} = \boldsymbol{\sigma}^{\text{eq}} + \boldsymbol{\sigma}^{\text{neq}}, \quad (15)$$

where

$$\begin{aligned} \boldsymbol{\sigma}^{\text{eq}} &= \frac{1}{J} \left( \frac{\mu^{\text{eq}}}{1-Q} \frac{I_m}{I_m - (I^N - 3)} \right) \left[ \mathbf{F} \mathbf{l}_0 \mathbf{F}^\top - \frac{3Q}{1+2Q} \text{sym}(\mathbf{d} \otimes \mathbf{F} \mathbf{l}_0 \mathbf{F}^\top \mathbf{d}) \right] - \left[ \frac{\mu^{\text{eq}}}{J} - \kappa(J-1) \right] \mathbf{I}, \\ \boldsymbol{\sigma}^{\text{neq}} &= \frac{1}{J} \left( \frac{\mu^{\text{neq}}}{1-Q} \frac{I_m}{I_m - (I^{Ne} - 3)} \right) \left[ \mathbf{F}^e \mathbf{l}_0 \mathbf{F}^{e\top} - \frac{3Q}{1+2Q} \text{sym}(\mathbf{d} \otimes \mathbf{F}^e \mathbf{l}_0 \mathbf{F}^{e\top} \mathbf{d}) \right] - \frac{\mu^{\text{neq}}}{J} \mathbf{I}. \end{aligned} \quad (16)$$

Similarly, substituting equations (10) and (11) into (13) gives the viscoelastic flow rule:

$$\mathbf{L}^v = \frac{\mu^{\text{neq}}}{\eta_N} \left( \frac{I_m}{I_m - (I^{Ne} - 3)} \mathbf{F}^{e\top} \mathbf{l}^{-1} \mathbf{F}^e \mathbf{l}_0 - \mathbf{I} \right). \quad (17)$$

For director rotation, substituting equations (10) and (11) into (14) gives:

$$\dot{\mathbf{d}} = \mathbf{W} \mathbf{d} - \frac{1}{J \eta_D} (\mathbf{m}^{\text{eq}} + \mathbf{m}^{\text{neq}}) + \frac{\gamma}{J \eta_D} (\mathbf{d} \cdot \mathbf{d} - 1)^2 \mathbf{d}, \quad (18)$$

where,

$$\begin{aligned} \mathbf{m}^{\text{eq}} &= -\mu^{\text{eq}} \frac{3Q}{(1-Q)(1+2Q)} \frac{I_m}{I_m - (I^N - 3)} [\mathbf{F} \mathbf{l}_0 \mathbf{F}^\top \cdot \mathbf{d} - (\mathbf{d} \cdot \mathbf{F} \mathbf{l}_0 \mathbf{F}^\top \cdot \mathbf{d}) \mathbf{d}] \\ \mathbf{m}^{\text{neq}} &= -\mu^{\text{neq}} \frac{3Q}{(1-Q)(1+2Q)} \frac{I_m}{I_m - (I^{Ne} - 3)} [\mathbf{F}^e \mathbf{l}_0 \mathbf{F}^{e\top} \cdot \mathbf{d} - (\mathbf{d} \cdot \mathbf{F}^e \mathbf{l}_0 \mathbf{F}^{e\top} \cdot \mathbf{d}) \mathbf{d}], \end{aligned} \quad (19)$$

The evolution of director viscosity is:

$$\eta_D = \eta_{D_0} \exp\left(-\frac{\sqrt{\boldsymbol{\sigma} : \boldsymbol{\sigma}}}{k_S}\right). \quad (20)$$

The dissipation power density for the model is given by:

$$\mathcal{D}_{\text{int}} = \eta_N \frac{\|\mathbf{L}^v\|^2}{J} + \eta_D \|\dot{\mathbf{d}}\|^2, \quad (21)$$

where the first term represents network dissipation and the second term represents dissipation from director rotation. The model was implemented as a UEL subroutine (Jiang, 2025) in Abaqus/Standard for finite element simulations of LCE structures.

The model includes eight parameters:  $Q$ ,  $\mu^{\text{eq}}$ ,  $\mu^{\text{neq}}$ ,  $\eta_N$ ,  $\eta_{D_0}$ ,  $k_S$ ,  $I_m$ , and  $\theta_0$ . These parameters were calibrated using the rate-dependent uniaxial stress response for the two sets

of monodomain LCEs with different crosslinking densities, stretched perpendicular to the initial director, as discussed in Section 2.1.4. The fitting process considered only the first 400% engineering strain, covering the semi-soft stress response. A preliminary study showed that the horizontal LCE bar of the unit cell structures did not stretch beyond 400% strain. The parameter calibration process using a material point program and the resulting table of parameters are described in Appendix C.

### 2.2.3. Finite element simulation of uniaxial tension tests

The material point computations described in Appendix C neglect the influence of boundary-induced inhomogeneities near the grips, which can affect the mechanical response in uniaxial tension (Chehade et al., 2024; Shen, 2025). We performed full-scale finite element simulations of uniaxial tension tests for LCE strips with different crosslinking densities to account for these effects and validate the nonlinear viscoelastic material model under large deformations. A user-defined element (UEL) implementation of the nonlinear viscoelastic model developed by Wang et al. (Wang et al., 2022) was used (see Section 2.2.2). Model parameters were assigned accordingly: parameters in Table C1 for the less crosslinked network and Table C2 for the more crosslinked network.

The model geometry represented a rectangular strip measuring 30 mm in length ( $x$ ), 6.1 mm in width ( $y$ ), and 0.63 mm in thickness ( $z$ ), discretized using 24,000 eight-node hexahedral elements, each with eight integration points. The mesh resolution was 0.3 mm in  $x$ , approximately 0.2 mm in  $y$ , and 0.08 mm in  $z$ . Boundary conditions were applied by fully fixing the left surface in all directions. The right surface was constrained in the  $y$  and  $z$  directions and subjected to prescribed displacement in  $x$ . A displacement of 120 mm, corresponding to 400% engineering strain, was applied at an effective strain rate of 1%/s, followed by unloading at the same rate.

To suppress macroscopic shear deformation from director rotation near the grips and improve numerical stability, the initial director was assigned an alternating pattern along the  $y$ -direction (Shen, 2025; Chehade et al., 2024). Figure 2 illustrates the initial director field of the more crosslinked network. Adjacent rows of elements were assigned initial director angles of  $\pm 80^\circ$  relative to the  $x$ -axis. This alternating pattern reduced net shear without suppressing local director reorientation and allowed better convergence. The chosen angle matched the experimentally observed peak stress and is discussed further in Appendix C. During simulation, the applied displacement was recorded as the  $x$ -displacement of the right surface. The total reaction force was computed by summing the  $x$ -direction reaction forces at all nodes on that surface. Engineering stress was calculated as the total force divided by the undeformed cross-sectional area, and engineering strain was defined as the applied displacement divided by the gauge length.

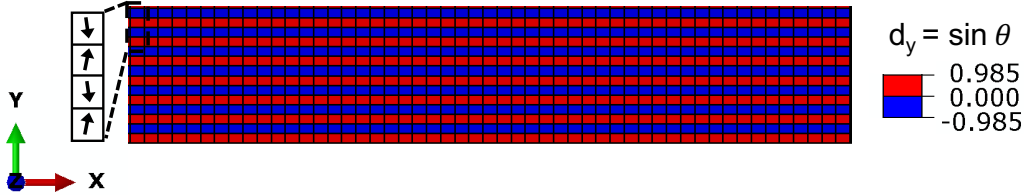


Figure 2: Finite element mesh with an alternating initial director pattern. The color scale represents the  $y$ -component of the initial director field,  $d_y = \sin \theta$ , where  $\theta$  is the initial director angle relative to the  $x$ -axis. Alternating strips are assigned  $\theta = \pm 80^\circ$ , corresponding to  $d_y = \pm 0.985$ .

#### 2.2.4. Finite element simulation of unit cell structures

We performed finite element simulations to analyze the mechanical response and energy dissipation of unit cell structures with varying horizontal member thicknesses and material properties. The unit cell geometry matched the experimental configuration (Section 2.1.2), consisting of four tilted LCE beams inclined at  $60^\circ$ , a horizontal transverse member, and rigid connectors (Figure 3).

The horizontal LCE bar (element block 1, red) was modeled using fully integrated eight-node hexahedral user-defined elements (UEs). The default material parameters corresponded to perpendicular LCEs with lower crosslinking density (Table C1); additional simulations used higher crosslinking density (Table C2). The nonlinear viscoelastic constitutive model included dissipation from mesogen rotation and polymer network viscoelasticity. Details of the micropolar viscoelastic model and parameter determination are provided in Section 2.2.2 and Appendix C, respectively.

The tilted LCE beams (element block 2, green) were modeled using fully integrated eight-node hybrid elements (C3D8H, Abaqus/Standard), incorporating the built-in finite-deformation viscoelastic model described in Section 2.2.1. Material parameters for polydomain LCEs with higher crosslinking density are listed in Table E1. Additional simulations with alternative beam orientations (parallel or perpendicular monodomain LCEs) were also conducted using relaxation spectra shown in Figure E4b.

Rigid joints (element block 3, grey) were assigned linear elastic properties ( $E = 10^4$  MPa,  $\nu = 0.4$ ) consistent with the experimental resin (Rigid 10K, Formlabs Inc., Somerville, MA, USA) and meshed using fully integrated eight-node hexahedral elements (C3D8, Abaqus/Standard).

The full finite element mesh contained 31,441 eight-node elements, including 4320 UEL elements in the horizontal bar and 3600 C3D8H elements per tilted beam (Figure 4). For the horizontal bar, element sizes were approximately 0.13 mm ( $x$ ), 0.42 mm ( $y$ ), and 0.11 mm ( $z$ ). For tilted beams, element sizes were approximately 0.268 mm along the beam axis, 0.155 mm transversely, and 0.42 mm through out-of-plane thickness ( $y$ ). Element sizes were selected based on a convergence study to ensure numerical accuracy. Boundary conditions are shown in Figure 3. The bottom surface was fixed, and lateral surfaces were constrained to allow symmetric  $x$ -direction displacements. Out-of-plane ( $y$ -direction) motion of the rigid joints was restricted. A prescribed vertical displacement was applied to a rigid plate in three stages: loading, unloading, and post-unloading hold. Loading and unloading rates matched those used in experiments (Section 2.1.5), and the top plate was held in its initial position for

30 seconds following unloading to observe the viscoelastic recovery of the structures. Vertical reaction force and displacement of the top surface were recorded throughout.

For the tilted LCE beams modeled with built-in elements, total elastic strain energy, internal energy, and viscoelastic dissipation were extracted directly from Abaqus output. For the horizontal LCE bar modeled with UEL elements, a custom post-processing algorithm was developed to decompose the total energy into contributions from elastic storage, mesogen rotation, and polymer network dissipation. Total energy absorption was calculated by numerically integrating the load-displacement loop curve using the trapezoidal rule.

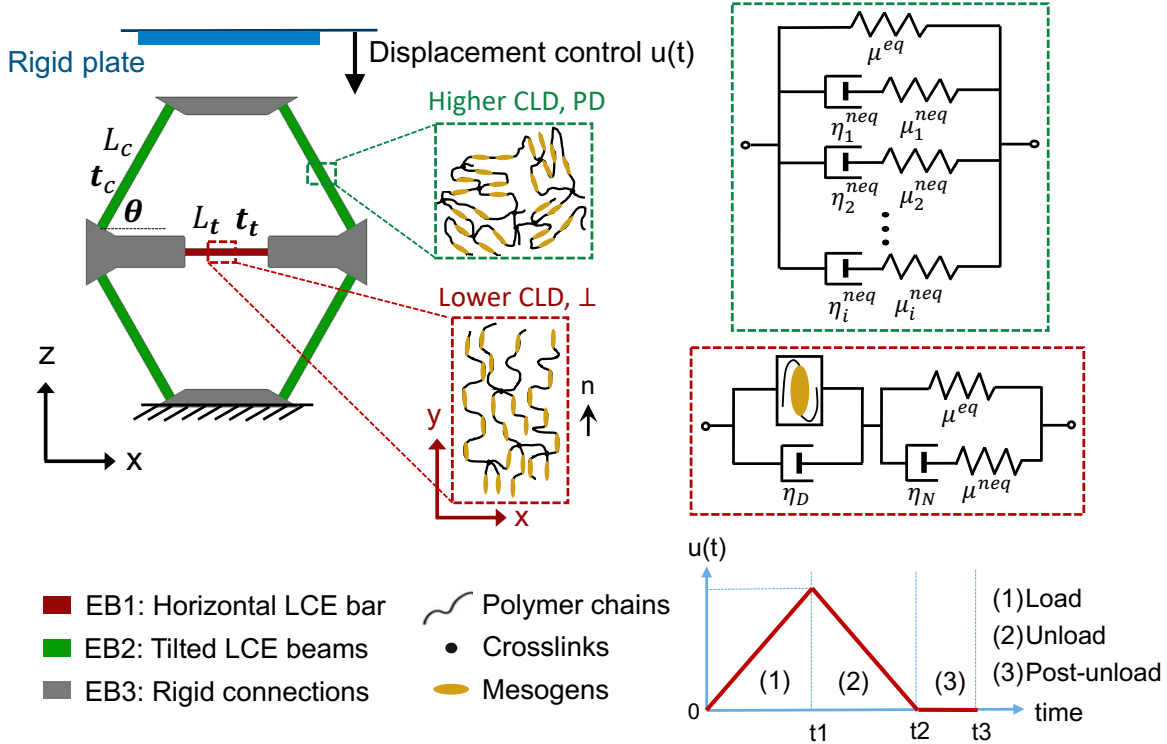


Figure 3: Schematic of the finite element model and boundary conditions. The unit cell includes a horizontal LCE bar (block 1, red), tilted LCE beams (block 2, green), and rigid joints (block 3, grey). A prescribed displacement  $u(t)$  was applied through a rigid plate, including loading, unloading, and a post-unload hold. Material models and geometric parameters are labeled.

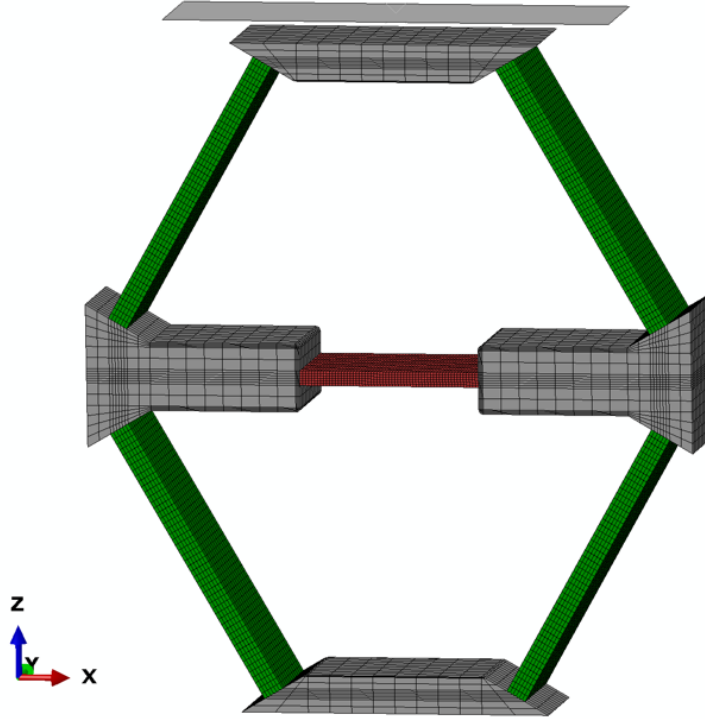


Figure 4: Finite element mesh of the unit cell structure.

### 3. Results and Discussions

#### 3.1. Finite deformation viscoelastic behavior of LCEs under uniaxial tension

We performed quasi-static uniaxial tension tests to investigate the finite-strain viscoelastic behavior of LCEs with varying crosslinking densities. Figure 5a-b compares engineering stress-strain responses from experiments, material point calculations, and FEA simulations for monodomain LCEs with initial director orientation perpendicular to the loading direction.

The less crosslinked LCEs exhibited a sharp stress drop after the peak, corresponding to rapid director rotation, whereas the more crosslinked samples showed smoother softening. Additional experimental results at other strain rates and for parallel specimens are presented in Figure B1 and discussed in Appendix B. All LCEs exhibited pronounced rate dependence, with nonzero residual strains and significant hysteresis upon unloading, confirming their potential for energy-dissipative applications. DMA measurements (Figures A1–A2, Appendix A) revealed  $\tan \delta > 0.5$  over a broad frequency range ( $10^1$ – $10^7$  rad/s), indicating strong viscoelastic damping.

Simulations captured key features of the experimental response, including peak stress and the soft stress plateau. The material point and FEA results closely agreed with each other. The parameters were fitted using experimental data up to 400% strain, which was sufficient to capture the plateau relevant to the horizontal LCE member deformation in the unit cell (Section 3.2). The model parameters are listed in Tables C1–C2. The fits were performed at a strain rate of 1%/s, and the model provided reasonable predictions across other rates (Figures C1–C2).

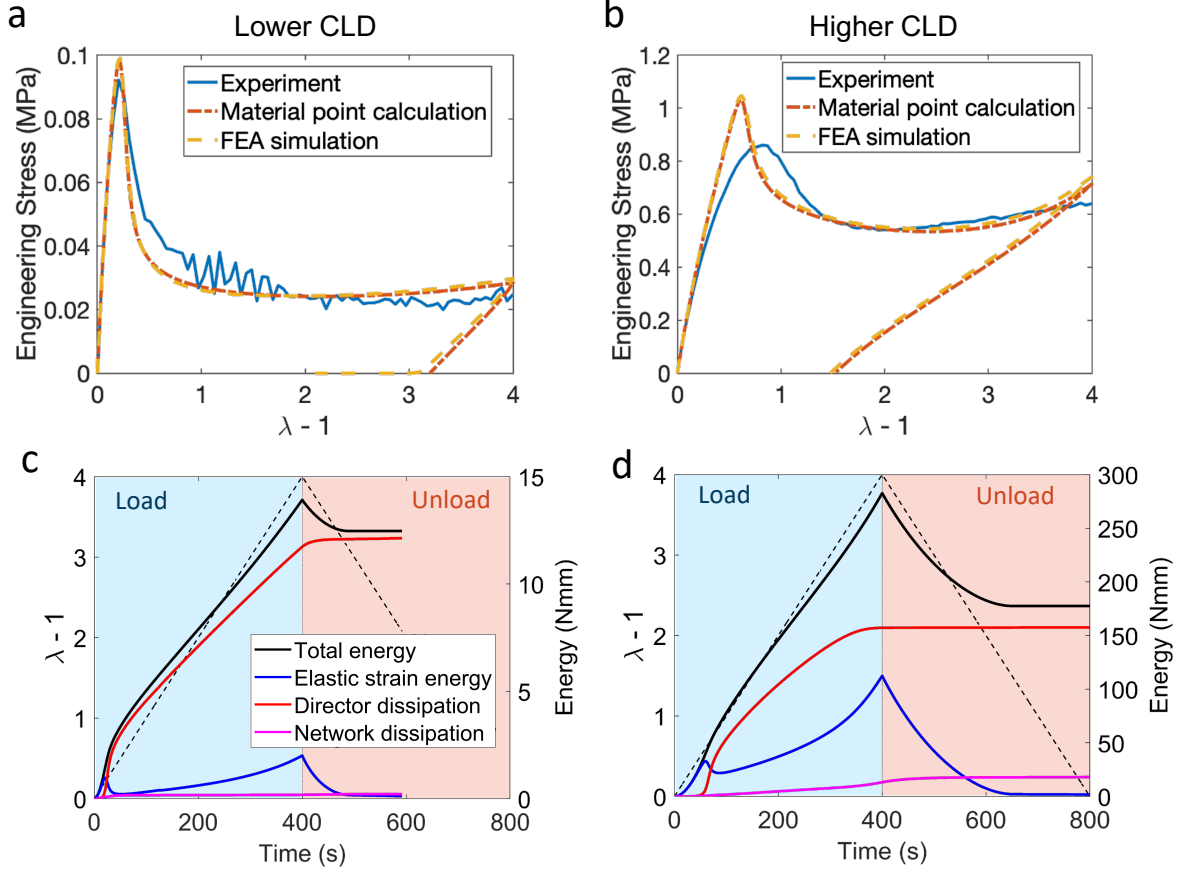


Figure 5: Uniaxial tension–unloading response at 1%/s for perpendicular LCEs with (a) lower and (b) higher crosslinking density (CLD), comparing experiment, material point calculation, and FEA simulation. (c, d) Corresponding energy contributions from FEA, showing elastic strain energy, network dissipation, and dissipation from director rotation. Here,  $\lambda$  is the stretch ratio. Dashed lines (left axis) indicate applied engineering strain ( $\lambda - 1$ ); energy components (right axis) share the same time axis.

The elastic strain energy and dissipation calculated for the FEA simulations are shown in Figure 5c-d. For both LCEs, elastic strain energy increased with applied stretch in the early stage. Dissipation from mesogen rotation remained negligible until soft stress activation, after which it rose sharply and eventually surpassed network dissipation. Upon unloading, elastic energy decreased, reflecting partial recovery, while mesogen dissipation remained constant, indicating irreversible rotation. Network dissipation continued to increase during unloading due to time-dependent stress relaxation. The more crosslinked LCE exhibited greater elastic energy storage and higher network dissipation. However, in both cases, dissipation from mesogen rotation was the dominant contributor to total energy loss. Increasing crosslinking density enhanced the stiffness of the network and its relative contribution to energy absorption.

### 3.2. Energy absorption of unit cell structures

Figure 6a compares deformation snapshots from compression tests and finite element simulations of unit cell 1 (Table 1) at a strain rate of 1%/s. The simulation colormap shows the

$x$ -component of the deformation gradient,  $F_{11}$ , in the horizontal LCE bar. Corresponding force–displacement curves are shown in Figure 6b. The use of a soft and highly stretchable LCE bar resulted in stretch-dominated deformation. Both the experimental and simulation results captured the elongation of the horizontal member and bending of the tilted LCE beams. The force–displacement response exhibited an initial linear relationship, followed by a peak and subsequent drop into a plateau. The decrease in the force can be attributed to the soft stress response of the horizontal LCE member. Upon unloading, the unit cell recovered the original shape, but the horizontal LCE member exhibit residual elongation from mesogen rotation. The elongation can be reversed by heating the unit cell above the nematic-isotropic transition temperature.

As shown in Figure 7f, the total energy dissipation was dominated by mesogen rotation in the stretched horizontal LCE bar, with additional contributions from viscoelastic bending in the tilted beams. The simulation slightly overestimated the peak force compared to experiments. In the experiments, the horizontal bar exhibited mild buckling during unloading, which was less pronounced than in the simulations. This discrepancy likely arises from differences in boundary conditions: in the experiments, lateral edges were unconstrained, resulting in more compliant deformation, whereas the simulations enforced symmetric displacements and rotational constraints, producing a stiffer response.

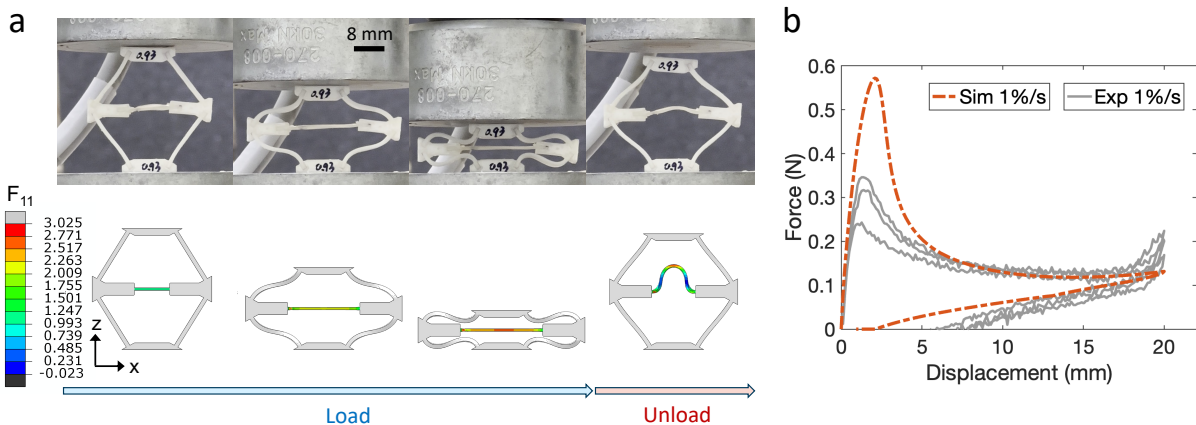


Figure 6: (a) Deformation snapshots from compression tests (top, unit cell 1) and finite element simulations (bottom) at a strain rate of 1%/s. The color map shows the deformation gradient component  $F_{11}$  in the horizontal LCE bar. (b) Corresponding force–displacement responses. Three replicate tests were conducted with thermal resetting before each run.

### 3.2.1. Effect of a stretchable LCE horizontal bar

Figure 7 compares the deformation and energy absorption behavior of unit cell structures with either a rigid or stretchable LCE horizontal bar, based on simulations and experiments conducted at strain rates of 1%/s, 10%/s, and 50%/s.

In the rigid-bar structure (Figure 7a, c, e), deformation was governed by buckling of the tilted LCE beams, consistent with prior work (Jeon et al., 2022). Initial loading produced a steep force increase, followed by buckling-induced softening and a secondary force peak near

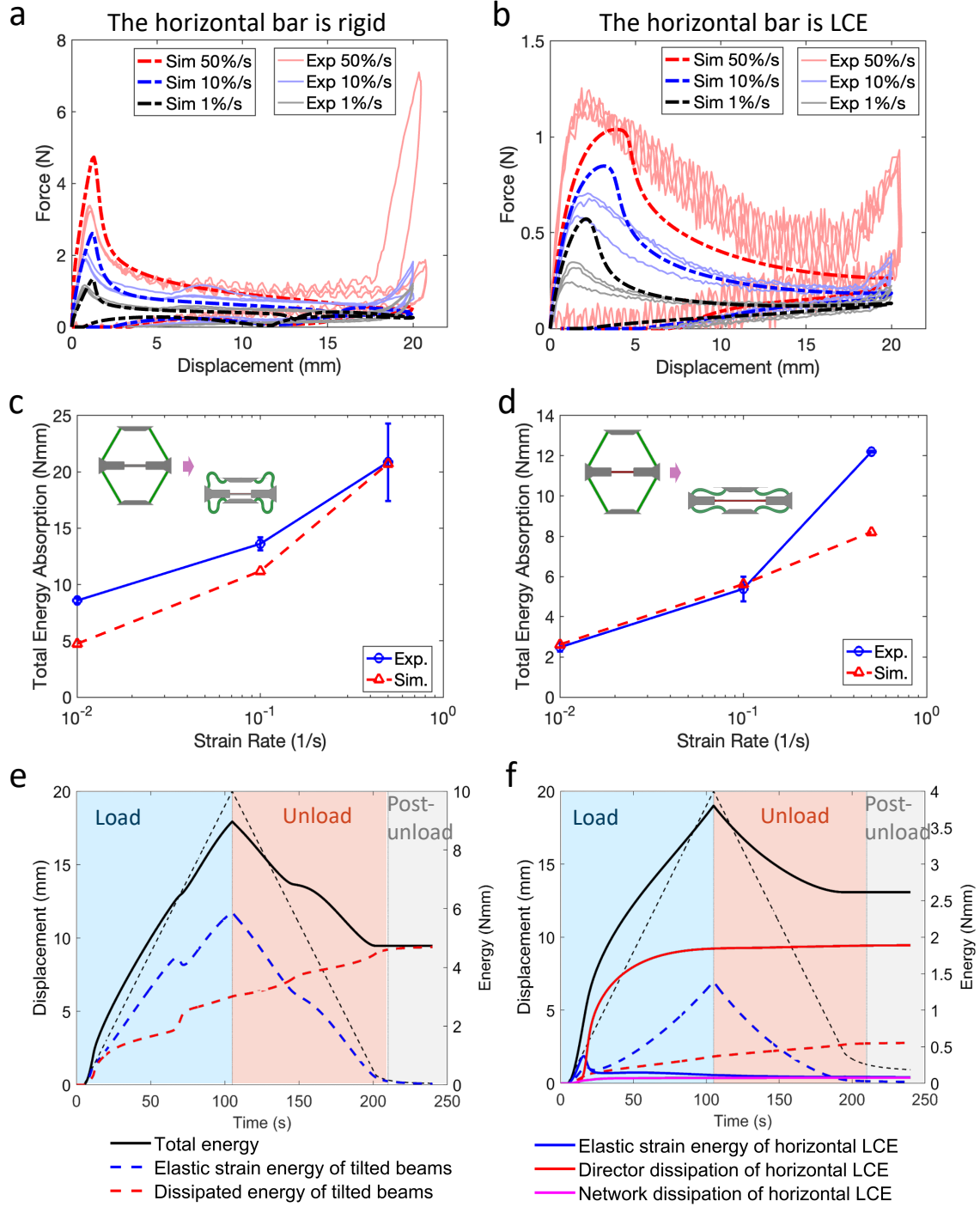


Figure 7: Experimental and simulation results for unit cell structures under compression at strain rates of 1%/s, 10%/s, and 50%/s. (a, c, e) Rigid-bar structure; (b, d, f) stretchable LCE-bar structure. Solid curves represent experiments; dashed curves represent simulations. In (e) and (f), black dashed lines (left axis) show applied displacement, and colored curves (right axis) indicate simulated energy contributions at 1%/s, including elastic storage, viscoelastic bending, and dissipation from director rotation.

full compression. Energy dissipation primarily arose from viscoelastic bending of the tilted

beams, which underwent buckling but ultimately recovered due to viscoelastic relaxation. Simulations captured the overall force–displacement trends, though peak forces were slightly overestimated, particularly at higher strain rates. At 50%/s, the abrupt increase in the force near the end of loading in experiments was attributed to contact between buckled beams and horizontal supports, enabled by lateral motion and minor geometric asymmetries. Simulated energy absorption showed qualitative agreement with experiments, with viscous dissipation reaching approximately 4.7 N·mm at 1%/s.

In contrast, the compliant LCE horizontal bar in the stretching-dominated structure (Figure 7b, d, f) elongated significantly, while the tilted beams bent without buckling. This produced a lower peak force followed by a broad plateau. A small rise in the force near the end of loading at 50%/s was again observed in experiments due to contact with the supports. The simulation results for the force-displacement response and the energy absorption of both unit cell structures agreed well with experiments. The simulation results for the energy absorption at the highest rate 50%/s for the stretchable unit cell underestimated the experimental data. The model only used a single relaxation process to describe the viscoelastic network behavior of the LCE horizontal member. The network relaxation time was calibrated using data from low strain rate test (1%/s), and thus may not accurately capture the viscoelastic behavior at the highest strain rate of 50%/s.

Introducing a stretchable LCE bar fundamentally altered the dominant dissipation mechanisms of the unit cell. While mesogen rotation enabled a new dissipation mechanism, lateral expansion suppressed beam buckling and reduced viscoelastic bending. At 1%/s, the total energy absorption decreased from 4.7 N·mm (rigid-bar) to 2.5 N·mm (stretchable-bar). This highlights a key trade-off: stiff horizontal members promote buckling-driven energy absorption, whereas compliant ones enable tension-driven dissipation from mesogen rotation. Optimizing the balance between these mechanisms is essential for maximizing energy absorption and is explored in the next section.

### 3.2.2. Effect of horizontal bar thickness and material properties

As shown in Section 3.2.1, introducing a stretchable LCE horizontal bar adds energy dissipation via mesogen rotation but suppresses bending in the tilted beams, a competing dissipation mechanism. To explore this trade-off, we conducted a parametric study in which we varied the horizontal bar thickness  $t_t$  while holding all other geometric and material parameters constant.

Figure 8 shows the simulation results for the case with  $t_t = 3$  mm ( $t_t/t_c = 3.23$ ) under compression at 1%/s. At small displacements, deformation was dominated by bending of the tilted beams. This is evident in the plots for the energy dissipation (Figure 8b), which shows increases only in the elastic energy and viscous dissipation from the tilted beams. When the tilted beams were bent into contact with the rigid supports, further compression increased the stretch in the horizontal bar and activated director rotation and the soft stress response. From this point to the end of loading (stage (2) to (3)), both soft stress and bending-related dissipation increased concurrently. During unloading, the two layers of buckled beams recovered sequentially, causing the adjacent layers to exhibit a cyclic recovery and reloading behavior, consistent with our prior study (Jeon et al., 2022). This reduced the elastic strain

energy and increased viscous network dissipation contributions to the total energy. Simultaneously, the horizontal bar continued to stretch, adding further dissipation via director rotation. The combined effect yielded a total energy absorption of 13 N·mm, which was over 2.5 times that of the rigid-bar case, demonstrating the benefit of coupling both mechanisms.

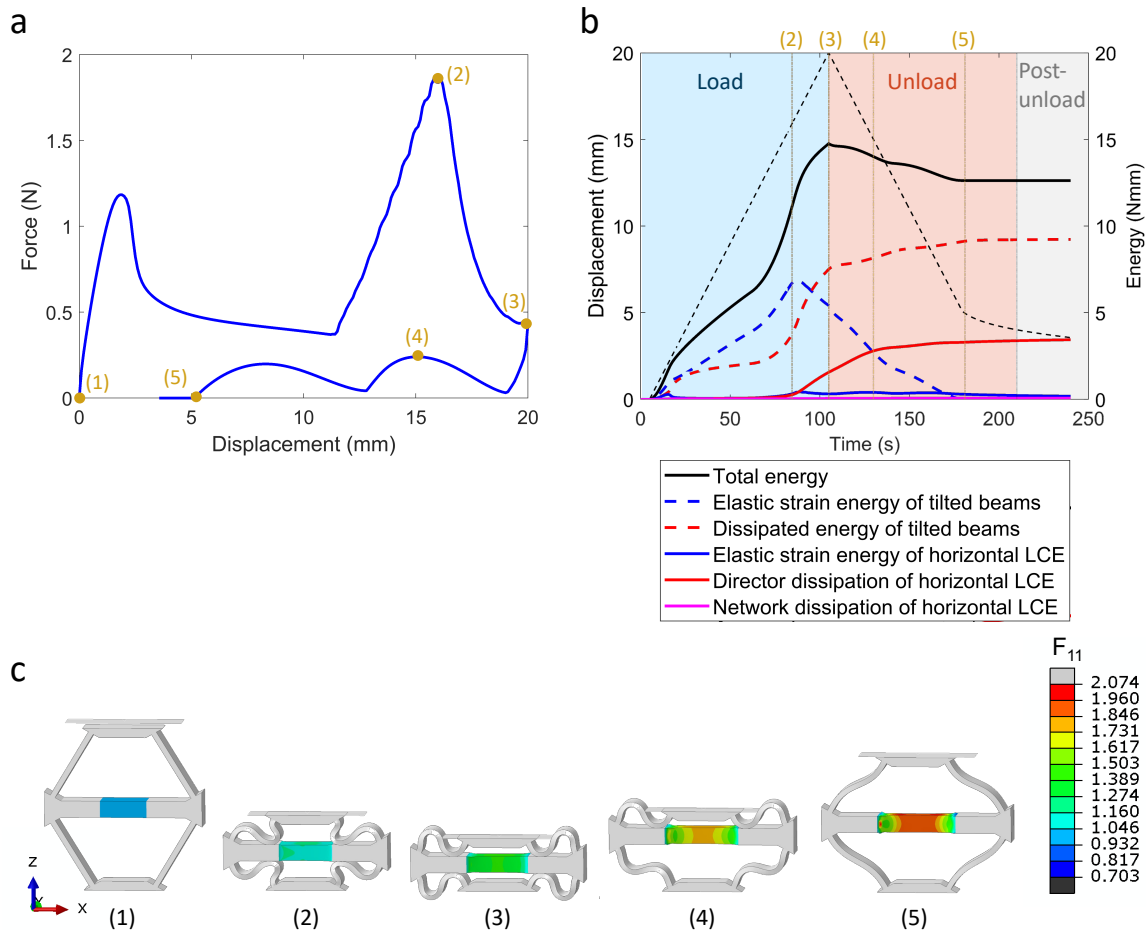


Figure 8: Finite element simulation of a unit cell structure with a 3 mm thick horizontal LCE bar ( $t_t/t_c = 3.23$ ) under compression at 1%/s. (a) Force–displacement curve. (b) Evolution of energy contributions from elastic storage, viscoelastic beam bending, and director rotation. The black dashed line indicates the applied displacement. (c) Deformation snapshots colored by the  $x$ -component of the deformation gradient ( $F_{11}$ ) in the horizontal LCE bar. Sequential activation of bending and soft stress enabled total energy absorption exceeding that of the rigid-bar case.

We repeated the simulation for varying ratios of the thickness of the horizontal bar and tilted beams  $t_t/t_c$ . As shown in Figure 9a, the energy absorption of the LCE-bar structure first increased with the thickness ratio. The energy absorption reached a maximum at  $t_t/t_c = 3$ , then decreased to equal the energy absorption of the rigid horizontal bar unit cell for  $t_t/t_c > 3$ . For small  $t_t/t_c$ , the LCE horizontal bar was too compliant, resulting in a stretch-dominated response with minimal bending of the tilted beams and, consequently, low energy absorption. In this regime, dissipation was dominated by director rotation in the horizontal bar, while energy dissipation from the tilted beams was very low. This is because the beams primarily

rotated with little bending to accommodate the large stretch of the thin horizontal bar. As  $t_t/t_c$  increased, the horizontal bar became stiffer, promoting greater bending in the tilted beams prior to the onset of director rotation and the associated soft stress response in the horizontal bar. This transition is reflected in the rising energy dissipation from both the tilted beams and the director rotation of the horizontal bar. This sequential activation of viscoelastic buckling and director rotation enabled the overall energy absorption of the stretchable horizontal-bar unit cell to exceed that of the rigid-bar structure by nearly a factor of three. Compared to smaller  $t_t/t_c$ , the dissipation of tilted beams contributed significantly more due to increased bending, while horizontal bar stretch remained sufficient to sustain high levels of dissipation from director rotation. The director rotation-induced dissipation peaked around  $t_t/t_c = 2$ . Beyond this point, further increases in bar stiffness enhanced beam buckling but reduced stretch in the horizontal bar, leading to a decline in director rotation and associated dissipation. As the horizontal bar became excessively stiff, it could no longer stretch enough to activate director rotation, causing this dissipation mode to diminish. Meanwhile, dissipation from the tilted beams gradually converged to that of the rigid-bar case. Note that network dissipation in the LCE horizontal bar was negligible at these strain levels, as director rotation dominated the response. However, if the bar were stretched beyond the soft stress regime, network dissipation would become more significant.

The normalized energy ratio  $E_{\text{LCE}}/E_{\text{Rigid}}$ , plotted in Figure 9b, shows that LCE-bar structures outperformed the rigid-bar baseline once  $t_t/t_c$  exceeded a threshold. The optimal ratio shifted to smaller values at lower strain rates, reflecting the interplay with viscoelasticity. Experimental results from unit cells 1, 3, and 5 qualitatively followed simulation trends. Deviations at larger  $t_t/t_c$  likely stemmed from boundary condition differences: lateral rotation and asymmetry occurred in experiments but were constrained in simulations.

To evaluate the effect of material properties in the tilted beams and horizontal bar, we repeated the analysis using a stiffer horizontal bar composed of perpendicular LCE with higher crosslinking density (parameters listed in Table C2). As shown in Figure 10, energy absorption retained a non-monotonic dependence on  $t_t/t_c$ , but the optimal ratio shifted to a lower value and the effective range narrowed due to the increased stiffness. Two experimental points are included for comparison. At  $t_t/t_c = 0$ , simulations and experiments showed good agreement. At higher  $t_t/t_c$ , simulations predicted symmetric buckling, whereas experiments exhibited rotation and asymmetric buckling of the tilted beams. This discrepancy is mainly attributed to boundary conditions: in simulations, the lateral edges of the unit cell were constrained against rotation, whereas in experiments, they were free to deform.

Overall, these parametric studies on horizontal bar thickness and material properties highlight the importance of tuning both geometry and material selection to balance viscoelastic bending and soft-stress tensile response for enhanced energy absorption.

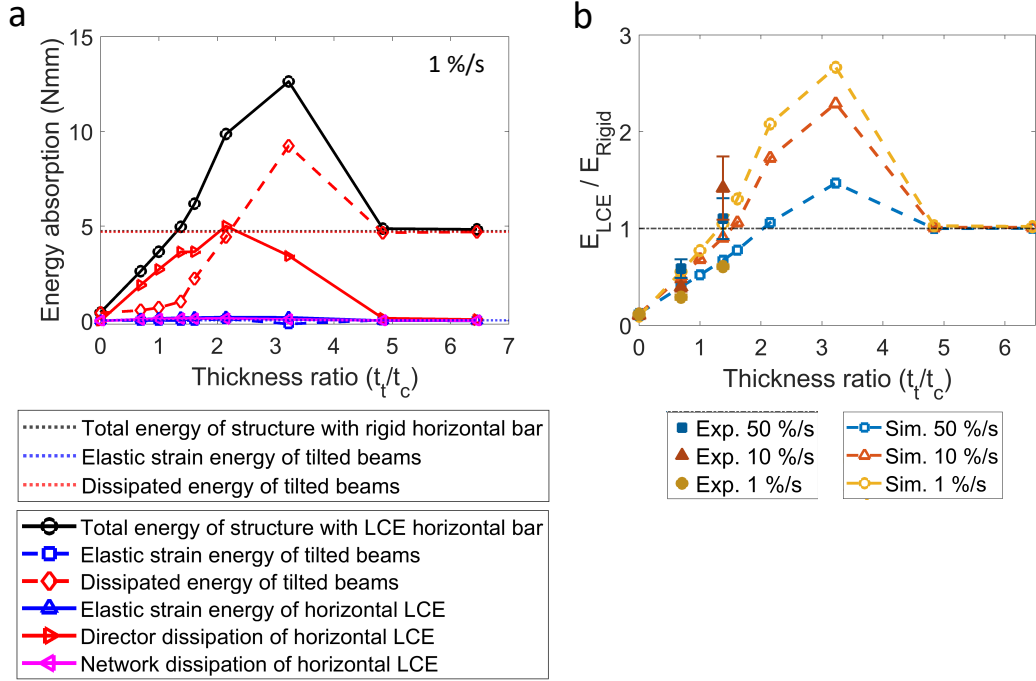


Figure 9: Effect of thickness ratio  $t_t/t_c$  between the horizontal and tilted beams on energy absorption. (a) Energy contributions for structures with a rigid bar (thin dotted lines) and stretchable LCE bar (thick lines), at 1%/s. The LCE-bar structure shows a non-monotonic dependence, peaking at intermediate  $t_t/t_c$ . (b) Normalized total energy absorption  $E_{LCE}/E_{Rigid}$  at 1%/s, 10%/s, and 50%/s. Open symbols: simulations; filled symbols: experiments. The optimal thickness ratio decreases at lower strain rates.

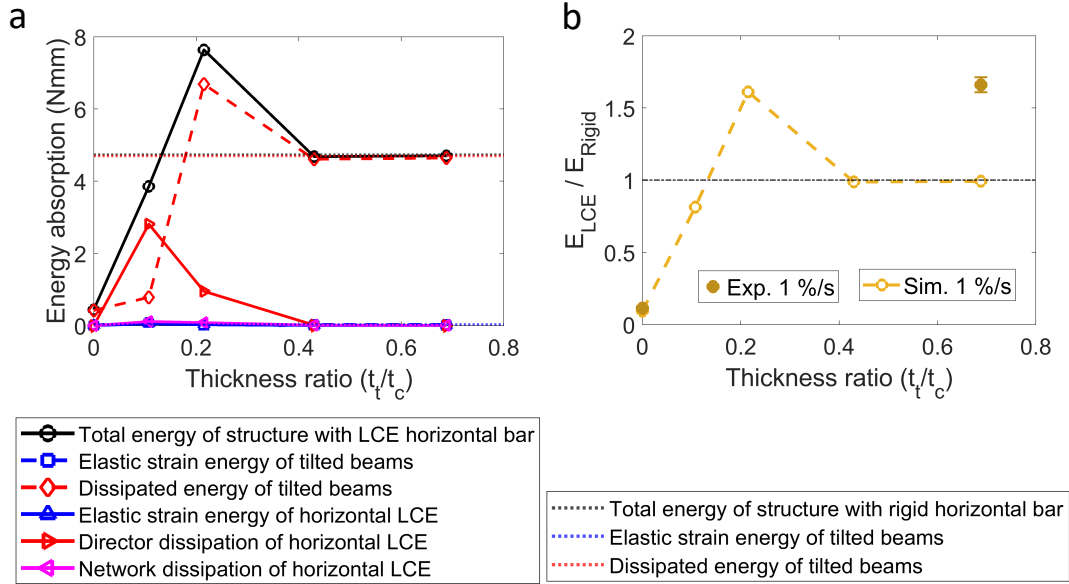


Figure 10: Effect of horizontal LCE bar material. (a) Energy absorption versus thickness ratio  $t_t/t_c$  for structures with either a rigid bar (thin dotted lines) or a stiffer perpendicular LCE bar (thick lines), at 1%/s. (b) Energy absorption ratio  $E_{LCE}/E_{Rigid}$ . Open circles: simulations; filled circles: experiments. Simulations show a non-monotonic trend with a narrower optimum for the stiffer LCE horizontal bar.

## 4. Conclusion

This study presents a novel strategy for enhancing energy dissipation in architected materials by leveraging the soft stress response of liquid crystal elastomers (LCEs). Specifically, we introduced stretchable LCE horizontal bars into hexagonal lattices with tilted LCE beams, enabling tension-induced mesogen rotation to contribute to dissipation under macroscopic compression.

We first characterized the finite-strain viscoelastic behavior of LCEs with varying crosslinking densities through dynamic mechanical analysis (DMA), uniaxial tension tests, and finite element simulations. Simulations employed a custom Abaqus UEL based on nonlinear viscoelastic theory for nematic LCEs, capturing the rate-dependent deformation and soft stress response. Dissipation in monodomain LCEs stretched into the soft stress plateau was dominated by viscous director rotation, while higher crosslinking densities led to stiffer responses, greater elastic energy storage, and enhanced network dissipation.

Building on prior work with rigid horizontal bars (Jeon et al., 2022), we introduced compliant LCE bars to activate dissipation via mesogen rotation under tensile deformation. However, this mechanism reduced beam bending by decreasing the tilt angle during compression, revealing a competition between the two modes. Through experiments and simulations, we demonstrated a non-monotonic dependence of energy absorption on the thickness ratio between horizontal and tilted beams. Thin bars promoted stretch-dominated deformation, whereas thick bars behaved as rigid constraints. At an intermediate, optimal ratio, sequential activation of viscoelastic beam bending followed by bar stretching yielded energy absorption 2–3 times greater than the rigid-bar case, exceeding the additive contributions of each mechanism. We further showed that increasing the crosslinking density in the horizontal bar shifted the optimal thickness ratio lower, and that lower strain rates enhanced energy dissipation and broadened the optimal design window.

These findings establish a design framework for coupling viscoelastic buckling with tension-driven soft stress in LCE-based lattices. By tuning geometric and material parameters, energy absorption can surpass that of conventional buckling instability-driven designs, with implications for impact mitigation, damping, and protective systems.

Several limitations remain. Simulated boundary conditions constrained lateral rotation, unlike the free deformation observed experimentally. Even in optimized cases, horizontal bar stretch remained limited, preventing full utilization of the soft stress regime. Parameters such as the stretchable bar length and beam tilt angle were not systematically explored. Snap-through buckling, which could trap elastic energy, was not investigated. Network dissipation in the horizontal bar was minimal at the applied strain levels but may be enhanced by designs that stretch beyond the soft stress regime. Nonetheless, to our knowledge, this is the first in-depth study to combine tension-induced mesogen rotation of LCEs with viscoelastic beam buckling in structural-level energy absorption. By revealing the interplay and competition between these mechanisms, this work lays a foundation for future exploration of LCE-based architected materials that extends beyond conventional design paradigms for energy absorption.

## **CRedit authorship contribution statement**

**Beijun Shen:** Conceptualization, Methodology, Investigation, Formal analysis, Software, Validation, Data Curation, Visualization, Writing - Original Draft, Writing - Review & Editing. **Yuefeng Jiang:** Software, Validation, Writing - Review & Editing. **Christopher M. Yakacki:** Conceptualization, Methodology, Writing - Review & Editing. **Sung Hoon Kang:** Conceptualization, Supervision, Funding acquisition, Writing - Review & Editing. **Thao D. Nguyen:** Conceptualization, Methodology, Resources, Supervision, Project administration, Funding acquisition, Writing - Review & Editing.

## **Declaration of competing interest**

The authors declare that they have no competing financial interests or personal relationships that could have appeared to influence the work reported in this paper.

## **Data availability**

Data will be made available on request.

## **Acknowledgements**

The authors would like to thank Prof. Sanjay Govindjee from the Department of Civil and Environmental Engineering at the University of California, Berkeley, for his insightful discussions and suggestions. B.S. gratefully acknowledges Dr. Alex Sun for his thoughtful guidance and unwavering support during challenging times. B.S. also thanks Dr. Tingting Xu and Mr. Bibekananda Datta for their valuable discussions and feedback. This work was supported in part by the Army Research Office (Grant Number W911NF-17-1-0165) (C.M.Y., S.H.K., T.D.N), Hanwha Non-tenured Faculty Award (S.H.K.), KAIST Start-Up Fund (S.H.K.), and Brain Pool Plus program through the National Research Foundation of Korea (NRF) funded by the Ministry of Science, ICT and Future Planning (award number: RS-2024-00439827) (S.H.K.).

## **A. Characterization of viscoelastic properties of LCEs**

Figure A1 shows the master curves of storage modulus and loss factor ( $\tan \delta$ ) for LCEs with varying crosslinking densities and director alignments. The storage modulus spanned over five orders of magnitude—from approximately  $10^{-1}$  to  $10^4$  MPa—across frequencies ranging from  $10^{-5}$  to  $10^{15}$  rad/s. LCEs with higher crosslinking density exhibited consistently higher moduli. Among different alignments, polydomain LCEs showed the lowest modulus at low frequencies under matched crosslinking conditions.

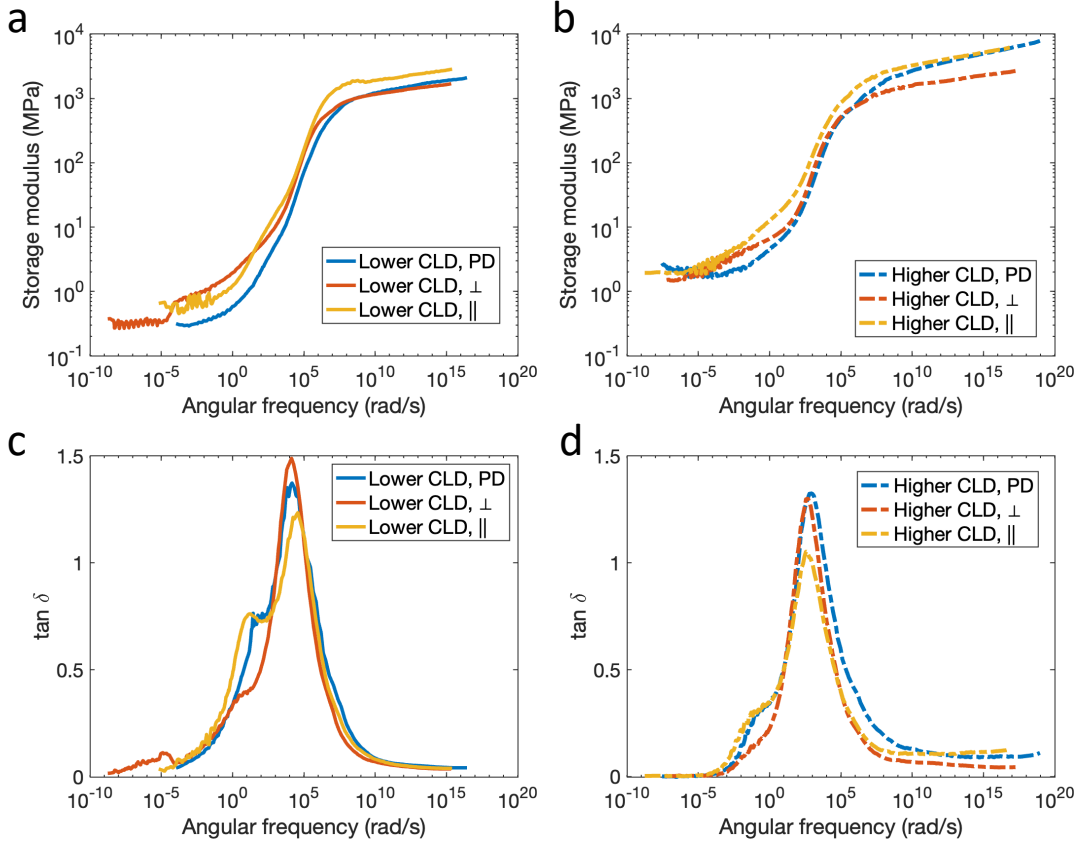


Figure A1: DMA characterization of polydomain (PD), perpendicular ( $\perp$ ), and parallel ( $\parallel$ ) LCEs. In  $\perp$  and  $\parallel$  samples, the initial director was aligned perpendicular or parallel to the loading direction, respectively. (a, b) Master curves of storage modulus for lower and higher crosslinking density. (c, d) Corresponding loss factor ( $\tan \delta$ ) curves. All data referenced to 25 °C.

All samples exhibited broad dissipation behavior, with  $\tan \delta$  exceeding 0.5 between  $10^1$  and  $10^7$  rad/s. LCEs with higher crosslinking density had reduced peak  $\tan \delta$  values and a shift to lower frequencies. A secondary peak with an extended shoulder was present across all samples, though it was smaller for more crosslinked networks. Parallel LCEs displayed lower primary  $\tan \delta$  peaks compared to polydomain and perpendicular counterparts, whereas their shoulder heights remained comparable to those of polydomain samples. Perpendicular samples showed the lowest shoulders. Figure A2 presents the corresponding temperature-dependent results. All LCEs showed characteristic transitions: a modulus drop near the glass transition temperature ( $T_g$ ), a broad dissipation peak between  $T_g$  and the nematic-to-isotropic transition temperature ( $T_{ni}$ ), and a secondary modulus drop near  $T_{ni}$  due to dynamic soft elasticity (Yakacki et al., 2015; Saed et al., 2016). Increasing crosslinking density raised both  $T_g$  and  $T_{ni}$ —from approximately 5 °C to 15 °C for  $T_g$ , and from 80 °C to 100 °C for  $T_{ni}$ —and increased moduli across all temperatures. These trends align with prior literature (Saed et al., 2017; Merkel et al., 2018; Traugutt et al., 2017; Saed et al., 2016).

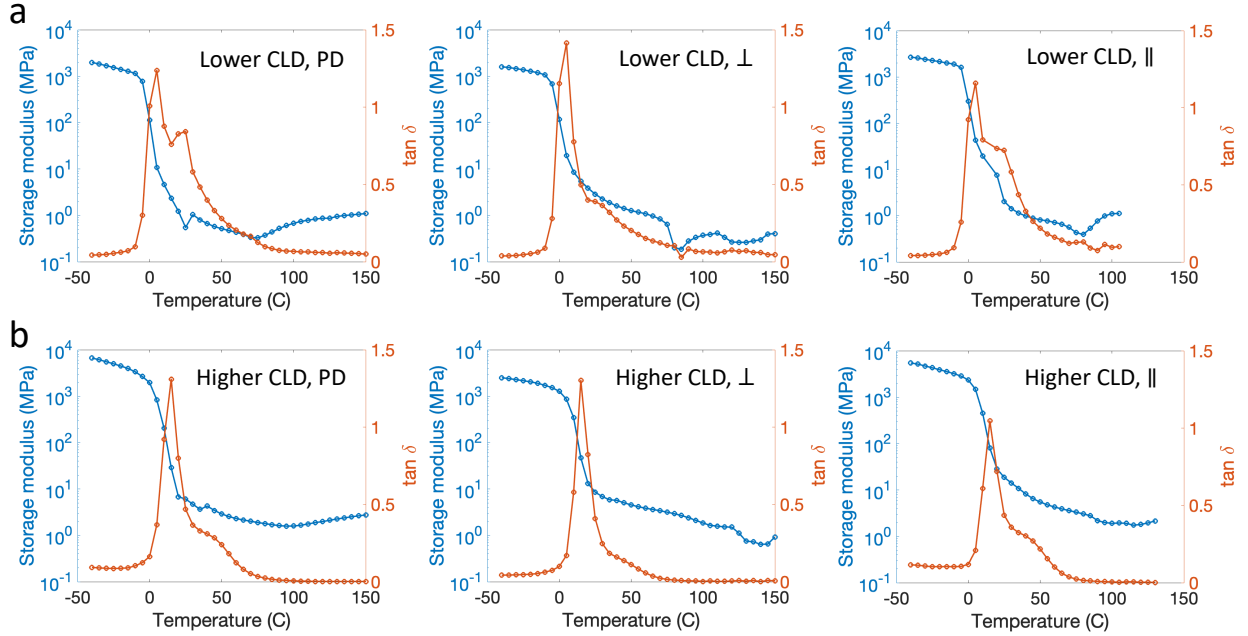


Figure A2: Storage modulus and  $\tan \delta$  vs. temperature at 0.93 Hz for LCEs with (a) lower and (b) higher crosslinking density (CLD).

## B. Finite-strain uniaxial tension load-unload tests of LCEs

Figure B1 shows the rate-dependent uniaxial stress–strain responses of perpendicular (a–b) and parallel (c–d) LCEs with different crosslinking densities (CLD). Variability across repeats was minimal; all specimens were thermally reset before testing. All LCEs exhibited pronounced strain rate dependence and retained residual strain after unloading. Recovery at room temperature occurred within 1–2 minutes for more crosslinked samples and 5–10 minutes for less crosslinked ones. Full recovery occurred immediately above  $T_{ni}$ .

Perpendicular LCEs showed an initial linear regime up to peak stress, followed by softening from mesogen rotation and stiffening from chain alignment. Less crosslinked samples exhibited a sharp stress drop after the peak, whereas more crosslinked ones showed smoother transitions. At the lowest rate (0.01%/s), forces in the low-CLD sample fell below the reliable detection limit of the 500 N load cell. Both peak and flow stresses increased with strain rate, consistent with stress-activated director rotation theory (Wang et al., 2022). The plateau widened at slower rates, and residual strain matched the plateau strain. Hysteresis increased with rate, especially in the stiffening region, indicating substantial polymer network viscoelasticity, supported by broad  $\tan \delta$  plateaus in Figures A1–A2. Parallel samples (Figure B1c–d) also showed rate-dependent behavior but lacked soft stress, as the directors were aligned with the loading axis. Dissipation was governed by network viscoelasticity, as indicated by load–unload hysteresis.

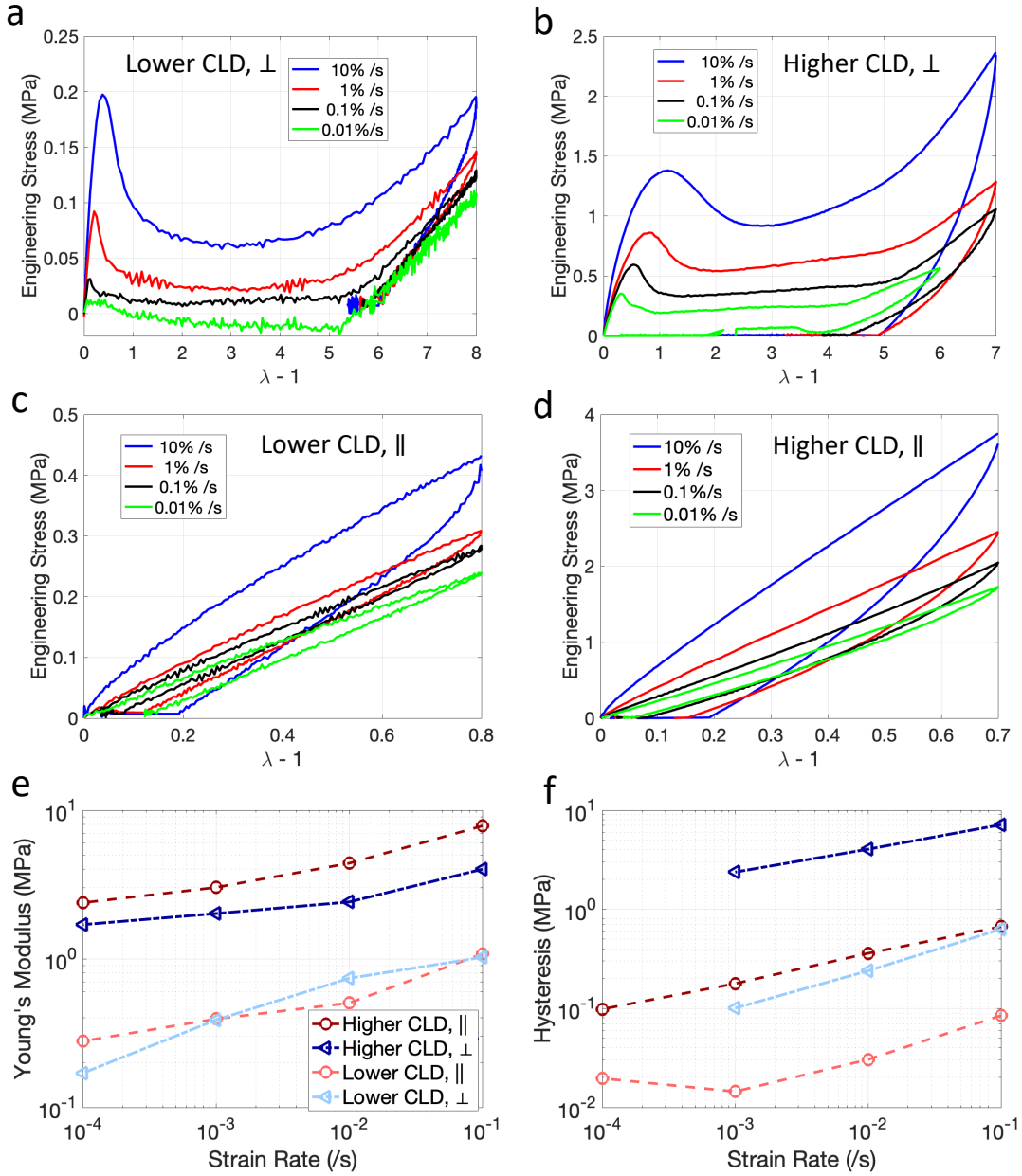


Figure B1: Uniaxial load–unload tests at varying strain rates for LCEs with different crosslinking densities (CLD). Engineering stress–strain responses for (a–b) perpendicular and (c–d) parallel LCEs. In the perpendicular and parallel configurations, the director is initially perpendicular or aligned with the loading direction. (e) Young’s modulus and (f) hysteresis as functions of strain rate. Stretch is denoted by  $\lambda$ .

Figures B1e–f quantify Young’s modulus and hysteresis as functions of strain rate. Both followed power-law scaling. Parallel LCEs were generally stiffer, especially in the high-CLD network where  $E_{\parallel} \approx 1.5\text{--}2E_{\perp}$ , consistent with prior reports (Martin Linares et al., 2020; Merkel et al., 2018). In contrast, low-CLD LCEs showed modest anisotropy. At 1%/s, some modulus estimates in the low-CLD group were less reliable due to near-threshold forces. Storage modulus trends from DMA (Figure A1) further support these anisotropic mechan-

ical responses. Hysteresis increased with strain rate across all conditions (Figure B1f), but comparison between perpendicular and parallel samples is complicated by different maximum strains. Perpendicular LCEs were extended into the mesogen rotation and strain-stiffening regimes, resulting in larger hysteresis. An outlier in the low-CLD parallel group at 0.01%/s may reflect noise at low force levels.

### C. Material point modeling and parameter fitting for perpendicular LCEs during uniaxial tension

To model the finite-strain, rate-dependent behavior of perpendicular LCEs, we employed the nonlinear viscoelastic framework developed by Wang et al. (Wang et al., 2022), which captures the coupling between director rotation and polymer network viscoelasticity. Material point simulations assumed homogeneous uniaxial deformation, enabling efficient parameter identification while retaining key physical mechanisms. Simulations were conducted at strain rates of 10%/s, 1%/s, 0.1%/s, and 0.01%/s for two LCEs with different crosslinking densities. Model predictions were compared to experimental results (Figures B1a-b).

Model parameters were calibrated by fitting the stress–strain response across all strain rates. For the lower-CLD LCE, the total instantaneous shear modulus  $\mu^{\text{eq}} + \mu^{\text{neq}} = 0.25$  MPa was obtained from the experimental Young’s modulus at 1%/s, assuming incompressibility. The director viscosity parameters  $\eta_{D_0} = 11$  MPa·s and  $k_S = 0.1$  were fitted to capture the draw stress at 10%/s, 1%/s, and 0.1%/s. The stiffening parameter  $I_m$  was set large to suppress chain stretch effects. The network viscosity  $\eta_N = 0.5$  MPa·s was fitted to the residual strain after unloading. The order parameter  $Q = 0.87$  controlled the soft plateau span, and the initial director angle  $\theta_0 = 83^\circ$  was selected to match the experimental peak stress.

A similar procedure was applied for the higher-CLD LCE. The instantaneous shear modulus was  $\mu^{\text{eq}} + \mu^{\text{neq}} = 0.8$  MPa. Director viscosity parameters  $\eta_{D_0} = 1000$  MPa·s and  $k_S = 0.6$  were fitted to the draw stress at various rates. A much larger  $\eta_N = 700$  MPa·s reflected the denser network. The order parameter  $Q = 0.62$  and director angle  $\theta_0 = 80^\circ$  were calibrated to match the soft plateau and peak stress, respectively. All fitted parameters are summarized in Tables C1 and C2.

Table C1: Model parameters for perpendicular LCE with lower crosslinking density (CLD).

Parameter	Physical significance	Value
$Q$	Order parameter	0.87
$\mu^{\text{eq}}$	Equilibrium shear modulus	0.20 MPa
$\mu^{\text{neq}}$	Nonequilibrium shear modulus	0.05 MPa
$\eta_N$	Network viscosity	0.5 MPa·s
$I_m$	Stiffening parameter	1000
$\eta_{D_0}$	Initial director viscosity	11 MPa·s
$k_S$	Viscosity evolution coefficient	0.1
$\theta_0$	Initial director angle	$83^\circ$
$\kappa$	Bulk modulus	4 MPa
$\gamma$	Penalty enforcing $\ \mathbf{d}\  = 1$	2

Table C2: Model parameters for perpendicular LCE with higher crosslinking density (CLD).

Parameter	Physical significance	Value
$Q$	Order parameter	0.62
$\mu^{\text{eq}}$	Equilibrium shear modulus	0.55 MPa
$\mu^{\text{neq}}$	Nonequilibrium shear modulus	0.25 MPa
$\eta_N$	Network viscosity	700 MPa·s
$I_m$	Stiffening parameter	10
$\eta_{D_0}$	Initial director viscosity	1000 MPa·s
$k_S$	Viscosity evolution coefficient	0.6
$\theta_0$	Initial director angle	$80^\circ$
$\kappa$	Bulk modulus	11 MPa
$\gamma$	Penalty enforcing $\ \mathbf{d}\  = 1$	2

Figures C1 and C2 compare simulation results to experimental curves. For the lower-CLD LCE, the model accurately captured the stress–strain response at all rates (Figure C1). For the higher-CLD LCE (Figure C2), simulations predicted a sharper peak and more pronounced softening than experiments, but reproduced key features such as the stress plateau, residual strain, and strain rate sensitivity. These results support the model’s fidelity in capturing the large-strain viscoelastic behavior of LCEs.

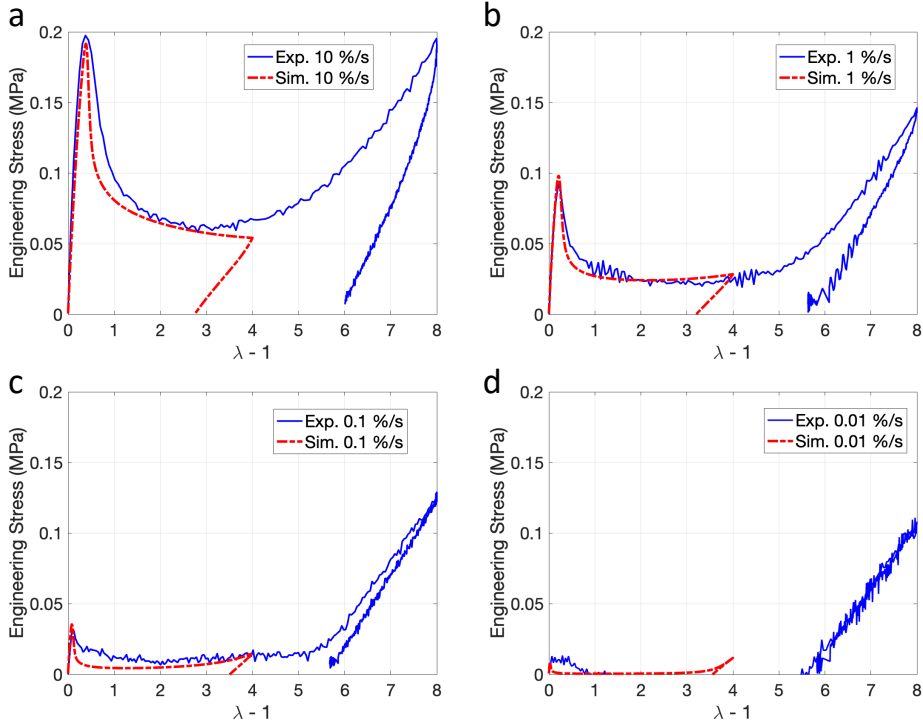


Figure C1: Material point simulations fitted to uniaxial tension responses of the perpendicular LCE with lower crosslinking density at strain rates of (a) 10%/s, (b) 1%/s, (c) 0.1%/s, and (d) 0.01%/s.

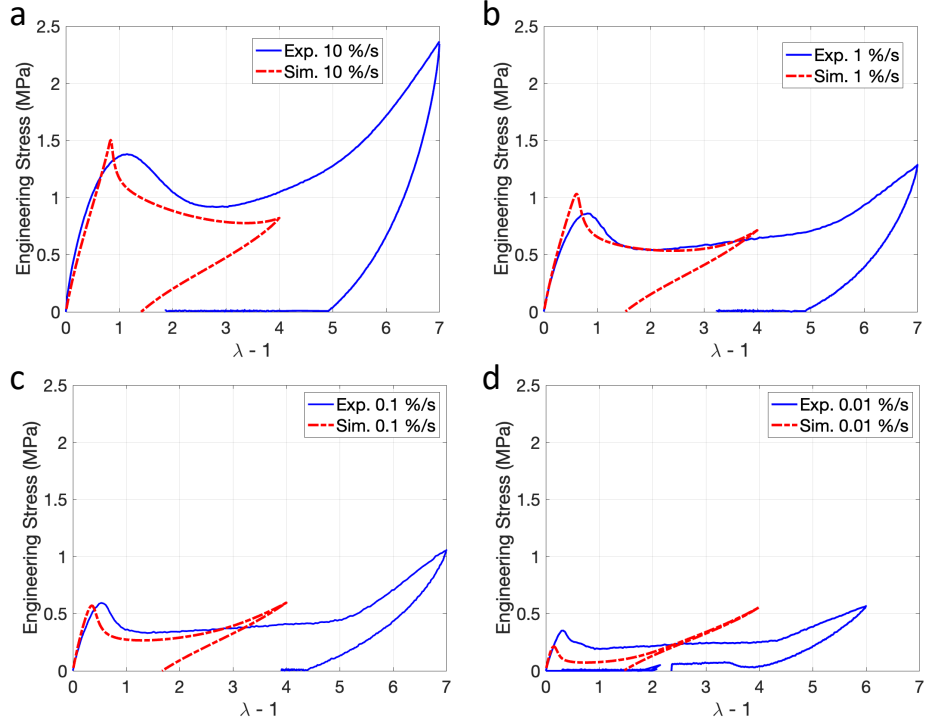


Figure C2: Material point simulations fitted to uniaxial tension responses of the perpendicular LCE with higher crosslinking density at strain rates of (a) 10%/s, (b) 1%/s, (c) 0.1%/s, and (d) 0.01%/s.

#### D. Validation of energy absorption computation during uniaxial tension simulations

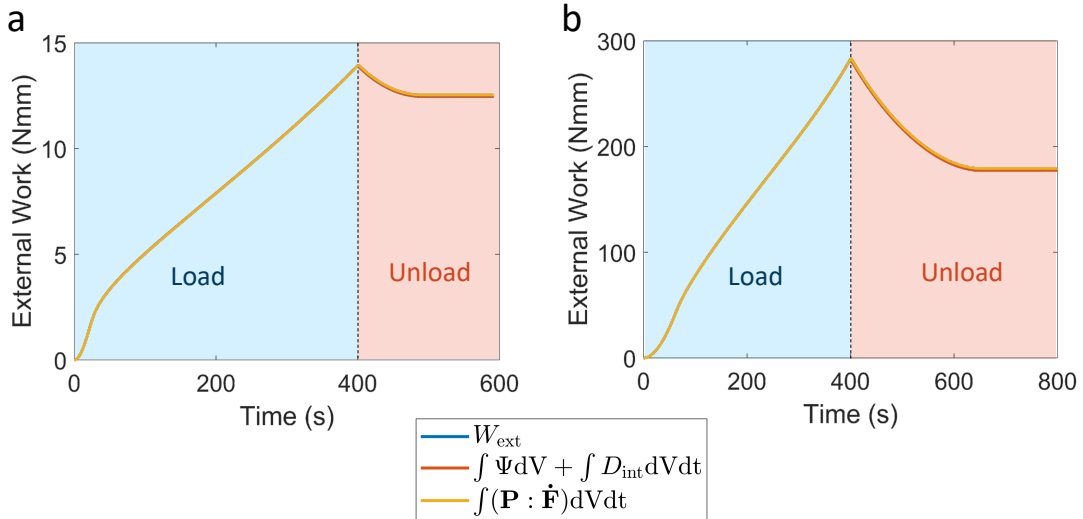


Figure D1: External work ( $W_{\text{ext}}$ ) computed by three methods from finite element simulations of uniaxial tensile load–unload cycles for perpendicular LCEs with (a) lower and (b) higher crosslinking density. Method 1: numerical integration of the force–displacement curve. Method 2:  $W_{\text{ext}} = \int \Psi dV + \int D_{\text{int}} dV dt$ , where  $\Psi$  is the Helmholtz free energy density and  $D_{\text{int}}$  is internal dissipation power per unit reference volume. Method 3:  $W_{\text{ext}} = \int (\mathbf{P} : \dot{\mathbf{F}}) dV dt$ , where  $\mathbf{P}$  is the first Piola–Kirchhoff stress and  $\dot{\mathbf{F}}$  is the deformation rate.

To ensure consistency in computing the external work during uniaxial tension simulations, we verified the results using three independent methods, as illustrated in Figure D1 for perpendicular LCEs with both crosslinking densities.

### E. Determining parameters for the finite-strain viscoelastic model

The storage modulus master curves (Figure A1a–b) were used to extract viscoelastic parameters for modeling the tilted LCE beams. Relaxation spectra ( $\tau_k, \mu_k^{\text{neq}}$ ) were obtained from the curves. For the polydomain LCE with higher crosslinking density, a fractional viscoelastic model was used to capture the experimental response with minimal fitting parameters (Haupt et al., 2000).

Following fractional calculus (Caputo and Mainardi, 1971; Koeller, 1984; Bagley and Torvik, 1986), the fractional derivative  $\frac{d^\alpha f}{dt^\alpha}$  for  $0 < \alpha < 1$  is defined as (Haupt et al., 2000):

$$\frac{d^\alpha f}{dt^\alpha} = \frac{1}{\Gamma(1-\alpha)} \int_0^t \frac{f'(s)}{(t-s)^\alpha} ds, \quad f(0) = 0, \quad (\text{E.1})$$

where  $\Gamma(\cdot)$  is the Gamma function. The fractional damping element (Lion, 1997; H Schiessel et al., 1995) relates stress to fractional strain rate:

$$\frac{d^\alpha \epsilon}{dt^\alpha} = \frac{\sigma}{E\zeta^\alpha}. \quad (\text{E.2})$$

Here,  $E$ ,  $\zeta$ , and  $\alpha$  are non-negative parameters. The model recovers Hookean and Newtonian behavior as  $\alpha \rightarrow 0$  and 1, respectively (Figure E1). Storage and loss moduli are given by (Haupt et al., 2000; Nguyen et al., 2010):

$$\begin{aligned} E'_{frac}(\omega) &= 3\mu^{\text{eq}} + \frac{2.7\mu^{\text{neq}}((\omega\zeta)^{2\alpha} + (\omega\zeta)^\alpha \cos(\alpha\pi/2))}{1 + (\omega\zeta)^{2\alpha} + 2(\omega\zeta)^\alpha \cos(\alpha\pi/2)}, \\ E''_{frac}(\omega) &= \frac{3\mu^{\text{neq}}(\omega\zeta)^\alpha \sin(\alpha\pi/2)}{1 + (\omega\zeta)^{2\alpha} + 2(\omega\zeta)^\alpha \cos(\alpha\pi/2)}. \end{aligned} \quad (\text{E.3})$$

The parameters  $\mu^{\text{eq}}$  and  $\mu^{\text{neq}}$  were estimated from the rubbery and glassy plateaus, assuming  $\nu_g = 0.35$  and  $\nu_r = 0.5$ . The fractional exponent  $\alpha$  controls the relaxation spectrum breadth, and  $\zeta$  sets the characteristic time scale. Fitting yielded  $\zeta = 3 \times 10^{-8}$  s and  $\alpha = 0.46$  (Figure E2). Deviations at high frequencies were considered negligible given the focus on moderate rates and lower frequencies.

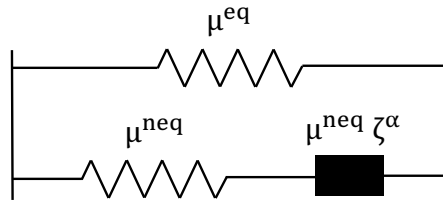


Figure E1: Fractional viscoelastic model with equilibrium and nonequilibrium shear moduli  $\mu^{\text{eq}}$ ,  $\mu^{\text{neq}}$ , spectral breadth  $\alpha$ , and characteristic relaxation time  $\zeta$ . Reproduced from (Haupt et al., 2000), with permission from Elsevier.

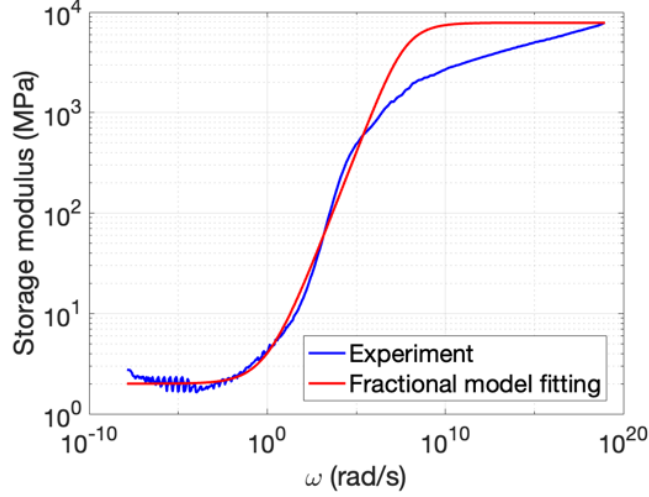


Figure E2: Storage modulus master curve fit using the fractional model at 25 °C.

The continuous relaxation spectrum is:

$$h_{\text{frac}}(\omega) = \frac{2.7\mu^{\text{neq}}(\omega\zeta)^\alpha \sin(\alpha\pi)}{\pi\omega [1 + (\omega\zeta)^{2\alpha} + 2(\omega\zeta)^\alpha \cos(\alpha\pi)]}. \quad (\text{E.4})$$

Its cumulative form is:

$$H_{\text{frac}}(\omega) = \int_0^\omega h_{\text{frac}}(z) dz, \quad (\text{E.5})$$

with analytic expression:

$$H_{\text{frac}}(\omega) = \frac{2.7\mu^{\text{neq}}}{\alpha\pi} \left[ \arctan \left( \frac{(\omega\zeta)^\alpha + \cos(\alpha\pi)}{\sin(\alpha\pi)} \right) - \pi \left( \frac{1}{2} - \alpha \right) \right]. \quad (\text{E.6})$$

Discrete relaxation frequencies were defined logarithmically:

$$\omega_k = \omega_{\text{min}} \left( \frac{\omega_{\text{max}}}{\omega_{\text{min}}} \right)^{\frac{k-1}{N-1}}, \quad \tau_k = 1/\omega_k. \quad (\text{E.7})$$

Discrete moduli  $\mu_i^{\text{neq}}$  were calculated to approximate  $H_{\text{frac}}(\omega)$ :

$$\begin{aligned} \mu_1^{\text{neq}} &= \frac{1}{2.7} \cdot \frac{1}{2} [H_{\text{frac}}(\omega_1) + H_{\text{frac}}(\omega_2)], \\ \mu_k^{\text{neq}} &= \frac{1}{2.7} \cdot \frac{1}{2} [H_{\text{frac}}(\omega_{k+1}) - H_{\text{frac}}(\omega_{k-1})], \quad 2 \leq k \leq N-1, \\ \mu_N^{\text{neq}} &= \mu^{\text{neq}} - \sum_{k=1}^{N-1} \mu_k^{\text{neq}}. \end{aligned} \quad (\text{E.8})$$

The final model used  $N = 20$  to balance accuracy and cost (Figure E3). Final parameters for the polydomain LCE with higher crosslinking density are summarized in Table E1, including relaxation times  $\tau_i^{\text{neq}}$ , shear moduli  $\mu_i^{\text{neq}}$ , viscosities  $\eta_i^{\text{neq}}$ , and the normalized Prony

series terms dimensionless shear (deviatoric)  $g_i$  and bulk (volumetric) moduli  $k_i$  for Abaqus (Dassault Systèmes, 2023).

Normalized moduli  $g_i$  are defined as:

$$g_i = \frac{\mu_i^{\text{neq}}}{\mu_0} = \frac{\mu_i^{\text{neq}}}{\sum_{i=1}^N \mu_i^{\text{neq}} + \mu^{\text{eq}}}, \quad (\text{E.9})$$

with  $\mu_0$  as the instantaneous shear modulus. Bulk relaxation was neglected by setting  $k_i = 0$ . The hyperelastic baseline used  $C_{10} = \mu^{\text{eq}}/2 = 0.333 \text{ MPa}$  and  $D_1 = 2/\kappa^{\text{eq}} = 2.29 \times 10^{-4}$ .

The same fitting procedure was applied to all six LCE types. Their fitted storage modulus curves and discrete spectra are shown in Figure E4.

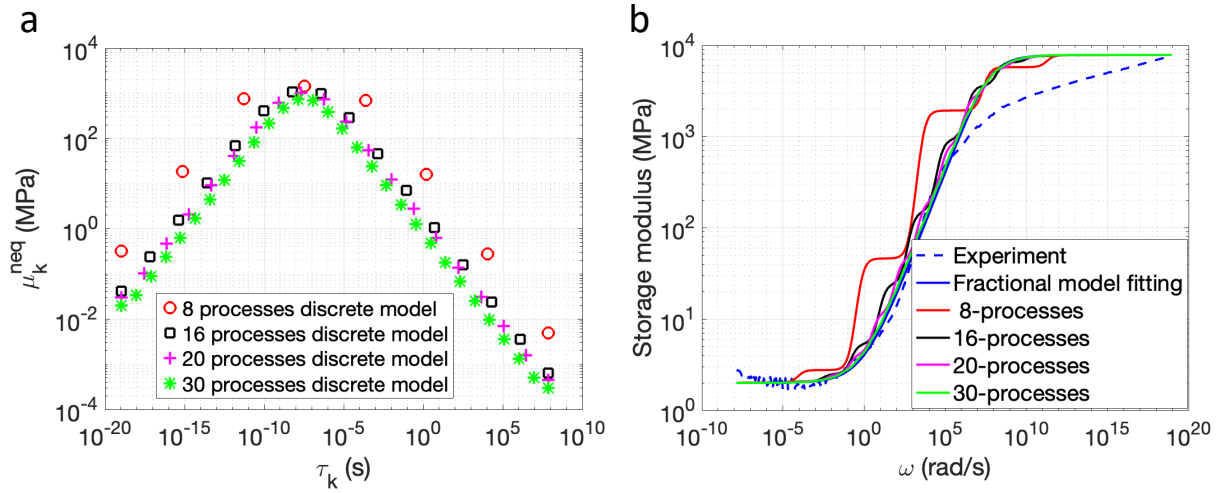


Figure E3: (a) Discrete relaxation spectra for different numbers of processes. (b) Reconstructed master curves of storage modulus for polydomain LCE with higher crosslinking density.

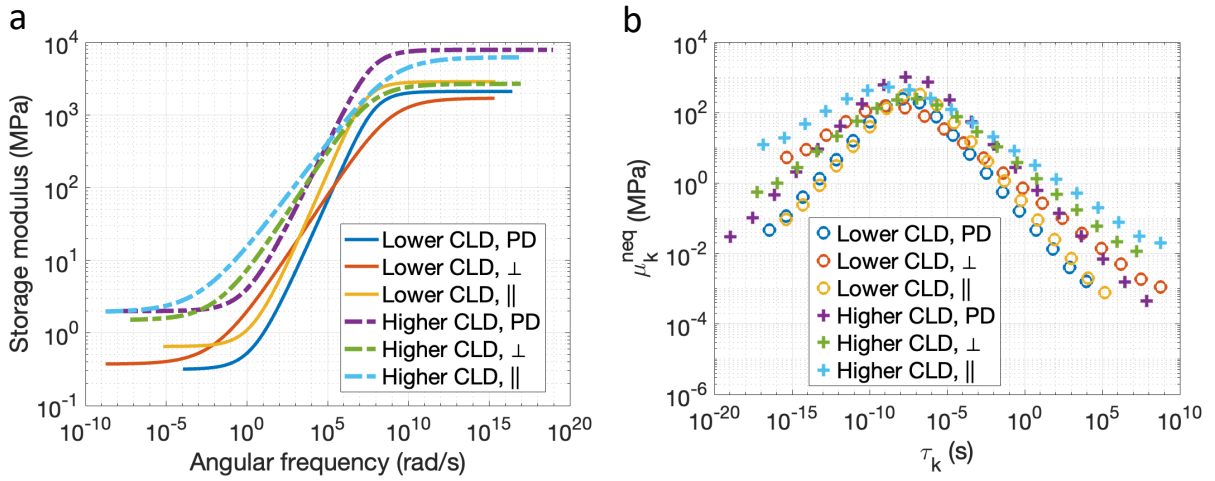


Figure E4: (a) Fractional model fits to storage modulus master curves for six LCE types. (b) Corresponding discrete relaxation spectra.

Table E1: Material parameters for modeling the polydomain LCE with higher crosslinking density.

Non-equilibrium branches	$\tau_i^{\text{neq}}$	$\mu_i^{\text{neq}}$	$\eta_i^{\text{neq}}$	$g_i$	$k_i$
1	$7.45 \times 10^7$	$4.51 \times 10^{-4}$	$3.36 \times 10^4$	$1.55 \times 10^{-7}$	0
2	$2.88 \times 10^6$	$1.56 \times 10^{-3}$	$4.51 \times 10^3$	$5.38 \times 10^{-7}$	0
3	$1.12 \times 10^5$	$6.98 \times 10^{-3}$	$7.79 \times 10^2$	$2.40 \times 10^{-6}$	0
4	$4.32 \times 10^3$	$3.11 \times 10^{-2}$	$1.35 \times 10^2$	$1.07 \times 10^{-5}$	0
5	$1.67 \times 10^2$	$1.39 \times 10^{-1}$	23.2	$4.78 \times 10^{-5}$	0
6	6.47	$6.20 \times 10^{-1}$	4.01	$2.13 \times 10^{-4}$	0
7	$2.51 \times 10^{-1}$	2.77	$6.93 \times 10^{-1}$	$9.52 \times 10^{-4}$	0
8	$9.70 \times 10^{-3}$	12.3	$1.20 \times 10^{-1}$	$4.24 \times 10^{-3}$	0
9	$3.75 \times 10^{-4}$	54.7	$2.05 \times 10^{-2}$	$1.88 \times 10^{-2}$	0
10	$1.45 \times 10^{-5}$	$2.33 \times 10^2$	$3.38 \times 10^{-3}$	$8.01 \times 10^{-2}$	0
11	$5.62 \times 10^{-7}$	$7.34 \times 10^2$	$4.13 \times 10^{-4}$	$2.53 \times 10^{-1}$	0
12	$2.18 \times 10^{-8}$	$1.02 \times 10^3$	$2.22 \times 10^{-5}$	$3.51 \times 10^{-1}$	0
13	$8.42 \times 10^{-10}$	$6.18 \times 10^2$	$5.21 \times 10^{-7}$	$2.13 \times 10^{-1}$	0
14	$3.26 \times 10^{-11}$	$1.76 \times 10^2$	$5.75 \times 10^{-9}$	$6.07 \times 10^{-2}$	0
15	$1.26 \times 10^{-12}$	40.8	$5.15 \times 10^{-11}$	$1.40 \times 10^{-2}$	0
16	$4.88 \times 10^{-14}$	9.18	$4.49 \times 10^{-13}$	$3.16 \times 10^{-3}$	0
17	$1.89 \times 10^{-15}$	2.06	$3.89 \times 10^{-15}$	$7.09 \times 10^{-4}$	0
18	$7.32 \times 10^{-17}$	$4.62 \times 10^{-1}$	$3.38 \times 10^{-17}$	$1.59 \times 10^{-4}$	0
19	$2.83 \times 10^{-18}$	$1.03 \times 10^{-1}$	$2.93 \times 10^{-19}$	$3.56 \times 10^{-5}$	0
20	$1.10 \times 10^{-19}$	$2.99 \times 10^{-2}$	$3.27 \times 10^{-21}$	$1.03 \times 10^{-5}$	0

## F. Finite element simulations of unit cell structures: effect of tilted LCE beam properties

Beyond the parametric studies on horizontal LCE bar thickness and material properties, we further examined how the viscoelastic behavior of the tilted LCE beams influences energy absorption in the hexagonal structure. This analysis aimed to clarify how beam material selection affects the balance between beam bending and bar stretching.

Prior to simulation, viscoelastic parameters for all six LCE types were extracted from DMA master curves and fitted using the fractional viscoelastic model described in Appendix E. The corresponding discrete relaxation spectra for  $N = 20$  non-equilibrium processes are shown in Figure E4.

We performed a parametric study using three LCE types—polydomain, perpendicular, and parallel—each with higher crosslinking density, as the material for the tilted beams. The horizontal LCE bar was fixed as a perpendicular LCE with lower crosslinking density (Figure F5a). Figures F5b–c show the simulation results. All cases exhibited stretch-dominant behavior, characterized by an initial force rise, a peak, and a sudden drop followed by a plateau, as previously observed in Figures 6 and 7b, d, f. Structural stiffness increased from polydomain to perpendicular to parallel LCEs. Dissipation from director rotation in the horizontal bar remained nearly constant, while viscoelastic bending dissipation increased

with beam stiffness, from lowest in polydomain to highest in parallel. These results indicate that, even with a fixed horizontal bar and stretch-dominant behavior, tilted beam properties significantly affect both force response and energy absorption.

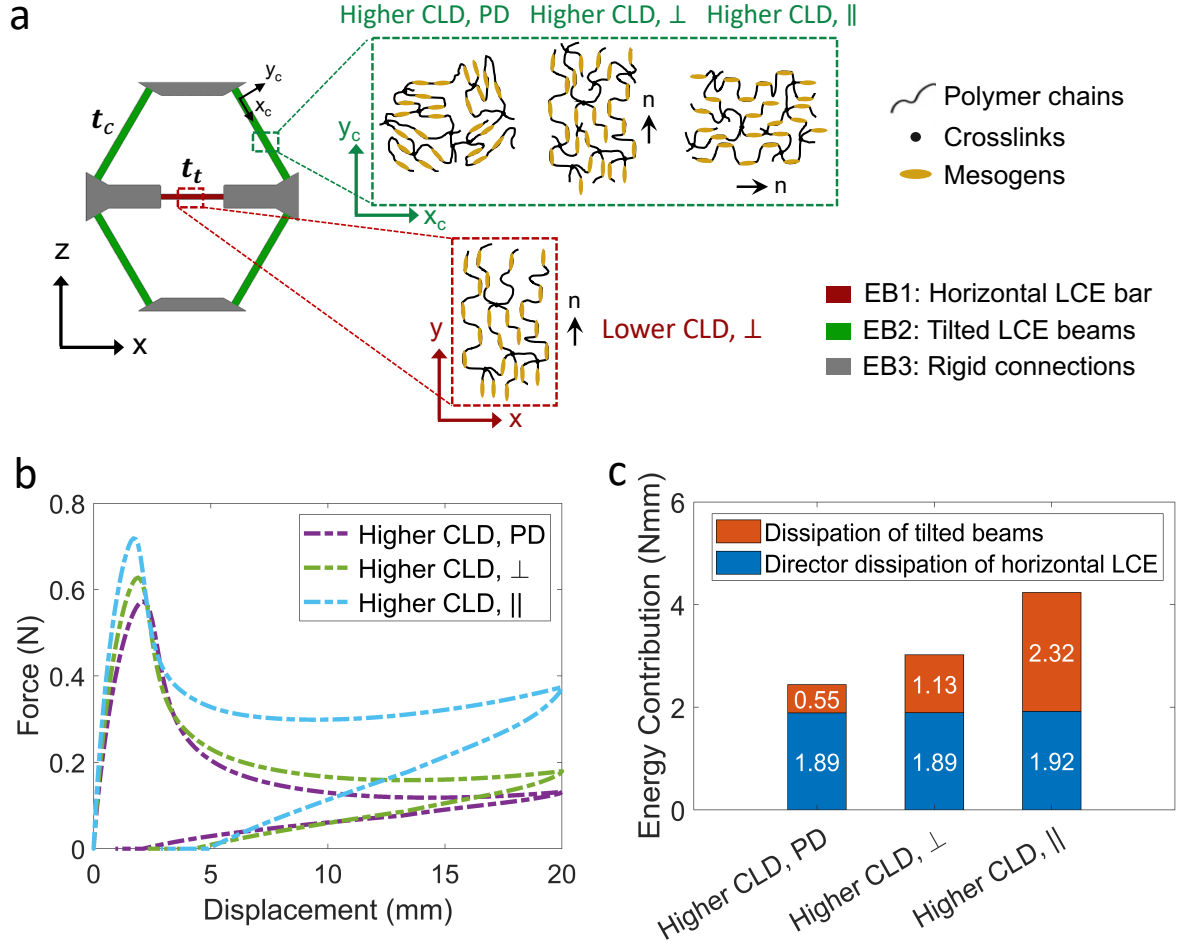


Figure F5: (a) Schematic of the unit cell structure with a horizontal LCE bar. The tilted beams are made from LCEs with higher crosslinking density (CLD): polydomain (PD), perpendicular ( $\perp$ ), or parallel ( $\parallel$ ). The horizontal bar is perpendicular LCE with lower CLD. (b) Simulated force–displacement curves using different tilted beam materials. (c) Corresponding energy contributions from beam bending and director rotation in the horizontal bar. Tilted beam and horizontal bar thicknesses are fixed at  $t_c = 0.93$  mm and  $t_t = 0.64$  mm, respectively.

## References

- S. Shan, S. H. Kang, J. R. Raney, P. Wang, L. Fang, F. Candido, J. A. Lewis, K. Bertoldi, Multistable Architected Materials for Trapping Elastic Strain Energy, *Advanced Materials* 27 (2015) 4296–4301. doi:[10.1002/ADMA.201501708](https://doi.org/10.1002/ADMA.201501708).
- L. R. Meza, S. Das, J. R. Greer, Strong, lightweight, and recoverable three-dimensional ceramic nanolattices, *Science* 345 (2014) 1322–1326. doi:[10.1126/science.1255908](https://doi.org/10.1126/science.1255908).

- Y. Chen, L. Jin, Reusable Energy-Absorbing Architected Materials Harnessing Snapping-Back Buckling of Wide Hyperelastic Columns, *Advanced Functional Materials* 31 (2021). doi:[10.1002/adfm.202102113](https://doi.org/10.1002/adfm.202102113).
- K. Bertoldi, Harnessing instabilities to design tunable architected cellular materials, *Annual Review of Materials Research* 47 (2017) 51–61. doi:[10.1146/annurev-matsci-070616-123908](https://doi.org/10.1146/annurev-matsci-070616-123908).
- H. Yang, L. Ma, Multi-stable mechanical metamaterials by elastic buckling instability, *Journal of Materials Science* 54 (2019) 3509–3526. doi:[10.1007/s10853-018-3065-y](https://doi.org/10.1007/s10853-018-3065-y).
- B. Haghpanah, L. Salari-Sharif, P. Pourrajab, J. Hopkins, L. Valdevit, Multistable Shape-Reconfigurable Architected Materials, *Advanced Materials* 28 (2016) 7915–7920. doi:[10.1002/adma.201601650](https://doi.org/10.1002/adma.201601650).
- T. Frenzel, C. Findeisen, M. Kadic, P. Gumbsch, M. Wegener, Tailored Buckling Microlattices as Reusable Light-Weight Shock Absorbers, *Advanced Materials* 28 (2016) 5865–5870. doi:[10.1002/adma.201600610](https://doi.org/10.1002/adma.201600610).
- J. Qiu, J. H. Lang, A. H. Slocum, A curved-beam bistable mechanism, *Journal of Microelectromechanical Systems* 13 (2004) 137–146. doi:[10.1109/JMEMS.2004.825308](https://doi.org/10.1109/JMEMS.2004.825308).
- S. Y. Jeon, B. Shen, N. A. Traugutt, Z. Zhu, L. Fang, C. M. Yakacki, T. D. Nguyen, S. H. Kang, Synergistic Energy Absorption Mechanisms of Architected Liquid Crystal Elastomers, *Advanced Materials* 34 (2022). doi:[10.1002/adma.202200272](https://doi.org/10.1002/adma.202200272).
- T. Liu, R. Deng, L. Jin, J. Cai, Rate-dependent and delayed snap-through behaviors of viscoelastic metamaterials, *International Journal of Mechanical Sciences* 283 (2024). doi:[10.1016/j.ijmecsci.2024.109664](https://doi.org/10.1016/j.ijmecsci.2024.109664).
- J. Li, Z. Chen, Q. Li, L. Jin, Z. Zhao, Harnessing Friction in Intertwined Structures for High-Capacity Reusable Energy-Absorbing Architected Materials, *Advanced Science* 9 (2022). doi:[10.1002/advs.202105769](https://doi.org/10.1002/advs.202105769).
- I. Valizadeh, O. Weeger, Rate-dependent energy dissipation of graded viscoelastic structures fabricated by grayscale vat photopolymerization, *Smart Materials and Structures* 33 (2024). doi:[10.1088/1361-665X/ad442a](https://doi.org/10.1088/1361-665X/ad442a).
- X. Yao, K. Liu, Q. Dong, X. Li, C. Ma, N. Hu, Tunable and recoverable energy absorption of foam-embedded architected cellular composite material at multiple strain rates, *Composite Structures* 329 (2024). doi:[10.1016/j.compstruct.2023.117745](https://doi.org/10.1016/j.compstruct.2023.117745).
- T. Liu, Y. Chen, J. W. Hutchinson, L. Jin, Buckling of viscoelastic spherical shells, *Journal of the Mechanics and Physics of Solids* 169 (2022). doi:[10.1016/j.jmps.2022.105084](https://doi.org/10.1016/j.jmps.2022.105084).
- M. Warner, E. M. Terentjev, International Series of Monographs on Physics Series Editors, 2003.

- J. Küupfer, H. Finkelmann, Liquid crystal elastomers: Influence of the orientational distribution of the crosslinks on the phase behaviour and reorientation processes, *Macromolecular Chemistry and Physics* 195 (1994) 1353–1367. doi:[10.1002/macp.1994.021950419](https://doi.org/10.1002/macp.1994.021950419).
- A. Azoug, V. Vasconcellos, J. Dooling, M. Saed, C. M. Yakacki, T. D. Nguyen, Viscoelasticity of the polydomain-monodomain transition in main-chain liquid crystal elastomers, *Polymer* 98 (2016) 165–171. doi:[10.1016/J.POLYMER.2016.06.022](https://doi.org/10.1016/J.POLYMER.2016.06.022).
- C. P. Martin Linares, N. A. Traugutt, M. O. Saed, A. Martin Linares, C. M. Yakacki, T. D. Nguyen, The effect of alignment on the rate-dependent behavior of a main-chain liquid crystal elastomer, *Soft Matter* 16 (2020) 8782–8798. doi:[10.1039/D0SM00125B](https://doi.org/10.1039/D0SM00125B).
- S. M. Clarke, A. R. Tajbakhsh, E. M. Terentjev, C. Remillat, G. R. Tomlinson, J. R. House, Soft elasticity and mechanical damping in liquid crystalline elastomers, *Journal of Applied Physics* 89 (2001) 6530–6535. doi:[10.1063/1.1368177](https://doi.org/10.1063/1.1368177).
- D. R. Merkel, R. K. Shaha, C. M. Yakacki, C. P. Frick, Mechanical energy dissipation in polydomain nematic liquid crystal elastomers in response to oscillating loading, *Polymer* 166 (2019) 148–154. doi:[10.1016/J.POLYMER.2019.01.042](https://doi.org/10.1016/J.POLYMER.2019.01.042).
- N. A. Traugutt, D. Mistry, C. Luo, K. Yu, Q. Ge, C. M. Yakacki, Liquid-Crystal-Elastomer-Based Dissipative Structures by Digital Light Processing 3D Printing, *Advanced Materials* 32 (2020). doi:[10.1002/adma.202000797](https://doi.org/10.1002/adma.202000797).
- B. Shen, Viscoelastic Behavior and Energy Absorption of Main-Chain Liquid Crystal Elastomers-Based Architected Materials, Ph.D. Dissertation, Johns Hopkins University, Baltimore, MD, USA, 2025.
- D. R. Merkel, N. A. Traugutt, R. Visvanathan, C. M. Yakacki, C. P. Frick, Thermomechanical properties of monodomain nematic main-chain liquid crystal elastomers, *Soft Matter* 14 (2018) 6024–6036. doi:[10.1039/c8sm01178h](https://doi.org/10.1039/c8sm01178h).
- S. M. Clarke, E. M. Terentjev, I. Kundler, H. Finkelmann, Texture Evolution during the Polydomain-Monodomain Transition in Nematic Elastomers, *Macromolecules* 31 (1998). doi:[10.1021/ma980195j](https://doi.org/10.1021/ma980195j).
- A. Takebe, K. Urayama, Supersoft elasticity and slow dynamics of isotropic-genesis polydomain liquid crystal elastomers investigated by loading- And strain-rate-controlled tests, *Physical Review E* 102 (2020). doi:[10.1103/PhysRevE.102.012701](https://doi.org/10.1103/PhysRevE.102.012701).
- D. Mistry, N. A. Traugutt, B. Sanborn, R. H. Volpe, L. S. Chatham, R. Zhou, B. Song, K. Yu, K. N. Long, C. M. Yakacki, Soft elasticity optimises dissipation in 3D-printed liquid crystal elastomers, *Nature Communications* 12 (2021). doi:[10.1038/s41467-021-27013-0](https://doi.org/10.1038/s41467-021-27013-0).
- A. Brinkmeyer, A. Pirrera, M. Santer, P. M. Weaver, Pseudo-bistable pre-stressed morphing composite panels, *International Journal of Solids and Structures* 50 (2013) 1033–1043. doi:[10.1016/j.ijsolstr.2012.11.019](https://doi.org/10.1016/j.ijsolstr.2012.11.019).

- M. Gomez, D. E. Moulton, D. Vella, Dynamics of viscoelastic snap-through, *Journal of the Mechanics and Physics of Solids* 124 (2019) 781–813. doi:[10.1016/j.jmps.2018.11.020](https://doi.org/10.1016/j.jmps.2018.11.020).
- K. Che, M. Rouleau, J. Meaud, Temperature-tunable time-dependent snapping of viscoelastic metastructures with snap-through instabilities, *Extreme Mechanics Letters* 32 (2019). doi:[10.1016/j.eml.2019.100528](https://doi.org/10.1016/j.eml.2019.100528).
- Y. Chen, T. Liu, L. Jin, Spatiotemporally Programmable Surfaces via Viscoelastic Shell Snapping, *Advanced Intelligent Systems* 4 (2022). doi:[10.1002/aisy.202100270](https://doi.org/10.1002/aisy.202100270).
- R. K. Shaha, D. R. Merkel, M. P. Anderson, E. J. Devereaux, R. R. Patel, A. H. Torbati, N. Willett, C. M. Yakacki, C. P. Frick, Biocompatible liquid-crystal elastomers mimic the intervertebral disc, *Journal of the Mechanical Behavior of Biomedical Materials* 107 (2020). doi:[10.1016/j.jmbbm.2020.103757](https://doi.org/10.1016/j.jmbbm.2020.103757).
- C. Luo, C. Chung, N. A. Traugutt, C. M. Yakacki, K. N. Long, K. Yu, 3D Printing of Liquid Crystal Elastomer Foams for Enhanced Energy Dissipation Under Mechanical Insult, *ACS Applied Materials & Interfaces* 13 (2021) 12698–12708. doi:[10.1021/acsami.0c17538](https://doi.org/10.1021/acsami.0c17538).
- H. Ye, Q. Liu, J. Cheng, H. Li, B. Jian, R. Wang, Z. Sun, Y. Lu, Q. Ge, Multimaterial 3D printed self-locking thick-panel origami metamaterials, *Nature Communications* 14 (2023). doi:[10.1038/s41467-023-37343-w](https://doi.org/10.1038/s41467-023-37343-w).
- A. L. Ruschel, F. W. Zok, A bi-material concept for periodic dissipative lattices, *Journal of the Mechanics and Physics of Solids* 145 (2020). doi:[10.1016/j.jmps.2020.104144](https://doi.org/10.1016/j.jmps.2020.104144).
- C. M. Yakacki, M. Saed, D. P. Nair, T. Gong, S. M. Reed, C. N. Bowman, Tailorable and programmable liquid-crystalline elastomers using a two-stage thiol-acrylate reaction, *RSC Advances* 5 (2015) 18997–19001. doi:[10.1039/C5RA01039J](https://doi.org/10.1039/C5RA01039J).
- M. O. Saed, A. H. Torbati, C. A. Starr, R. Visvanathan, N. A. Clark, C. M. Yakacki, Thiol-acrylate main-chain liquid-crystalline elastomers with tunable thermomechanical properties and actuation strain, *Journal of Polymer Science, Part B: Polymer Physics* 55 (2017) 157–168. doi:[10.1002/polb.24249](https://doi.org/10.1002/polb.24249).
- J. D. Ferry, *Viscoelastic properties of polymers*, Wiley, 1980.
- Dassault Systèmes, *SIMULIA User Assistance 2023: Abaqus*, 2023. URL: <https://help.3ds.com>.
- Z. Wang, A. El Hajj Chehade, S. Govindjee, T. D. Nguyen, A nonlinear viscoelasticity theory for nematic liquid crystal elastomers, *Journal of the Mechanics and Physics of Solids* 163 (2022). doi:[10.1016/j.jmps.2022.104829](https://doi.org/10.1016/j.jmps.2022.104829).
- Y. Jiang, Uel-micropolar-lce, 2025. URL: <https://github.com/Sooosad/UEL-Micropolar-LCE>.
- A. E. H. Chehade, B. Shen, C. M. Yakacki, T. D. Nguyen, S. Govindjee, Finite element modeling of viscoelastic liquid crystal elastomers, *International Journal for Numerical Methods in Engineering* 125 (2024). doi:[10.1002/nme.7510](https://doi.org/10.1002/nme.7510).

- M. O. Saed, A. H. Torbati, D. P. Nair, C. M. Yakacki, Synthesis of programmable main-chain liquid-crystalline elastomers using a two-stage thiol-acrylate reaction, *Journal of Visualized Experiments* 2016 (2016). doi:[10.3791/53546](https://doi.org/10.3791/53546).
- N. A. Traugutt, R. H. Volpe, M. S. Bollinger, M. O. Saed, A. H. Torbati, K. Yu, N. Dadvanyan, C. M. Yakacki, Liquid-crystal order during synthesis affects main-chain liquid-crystal elastomer behavior, *Soft Matter* 13 (2017) 7013–7025. doi:[10.1039/c7sm01405h](https://doi.org/10.1039/c7sm01405h).
- P. Haupt, A. Lion, E. Backhaus, On the dynamic behaviour of polymers under finite strains: constitutive modelling and identification of parameters, *International Journal of Solids and Structures* 37 (2000) 3633–3646. doi:[10.1016/S0020-7683\(99\)00165-1](https://doi.org/10.1016/S0020-7683(99)00165-1).
- M. Caputo, F. Mainardi, Linear models of dissipation in anelastic solids, *La Rivista del Nuovo Cimento* (1971-1977) 1 (1971) 161–198. doi:[10.1007/BF02820620](https://doi.org/10.1007/BF02820620).
- R. C. Koeller, Applications of Fractional Calculus to the Theory of Viscoelasticity, *Journal of Applied Mechanics* 51 (1984) 299–307. doi:[10.1115/1.3167616](https://doi.org/10.1115/1.3167616).
- R. L. Bagley, P. J. Torvik, On the Fractional Calculus Model of Viscoelastic Behavior, *Journal of Rheology* 30 (1986) 133–155. doi:[10.1122/1.549887](https://doi.org/10.1122/1.549887).
- A. Lion, On the thermodynamics of fractional damping elements, *Continuum Mechanics and Thermodynamics* 9 (1997) 83–96. doi:[10.1007/s001610050057](https://doi.org/10.1007/s001610050057).
- H Schiessel, R Metzler, A Blumen, T F Nonnenmacher, Generalized viscoelastic models: their fractional equations with solutions, *Journal of Physics A: Mathematical and General* 28 (1995) 6567. doi:[10.1088/0305-4470/28/23/012](https://doi.org/10.1088/0305-4470/28/23/012).
- T. D. Nguyen, C. M. Yakacki, P. D. Brahmhatt, M. L. Chambers, Modeling the relaxation mechanisms of amorphous shape memory polymers, *Advanced Materials* 22 (2010) 3411–3423. doi:[10.1002/adma.200904119](https://doi.org/10.1002/adma.200904119).